

## Theory of Magnetic and Structural Ordering in Iron

C. S. Wang

*Department of Physics and Astronomy, University of Maryland, College Park, Maryland 20742, and  
Condensed Matter Physics Branch, Naval Research Laboratory, Washington, D.C. 20375*

and

B. M. Klein

*Condensed Matter Physics Branch, Naval Research Laboratory, Washington, D.C. 20375*

and

H. Krakauer

*Department of Physics, College of William and Mary, Williamsburg, Virginia 23185*

(Received 10 October 1984)

Using the total-energy general-potential linearized-augmented-plane-wave method, we have tested the adequacy of the local-spin-density approximation for describing the magnetic and structural properties of iron. We find that there are fundamental deficiencies in the local-spin-density approximation, both quantitative and qualitative, in that there are substantial errors in the calculated ground-state volumes and magnetic moments, as well as a prediction of the wrong ground-state crystal structure.

PACS numbers: 71.45.Nt, 75.10.Lp

It has recently been established that the local-spin-density approximation (LSDA) within the density-functional theory can provide an accurate theoretical estimate of static structural properties, phonon spectra, crystal stability, and pressure-induced phase transformations in solids. These achievements are important because they establish a new approach for predicting, from first principles, the structural properties of more complicated systems where theoretical understanding has been limited to empirical methods and experimental data may be lacking. However, the limitations of the LSDA for magnetic materials, such as iron, are still open to question. In this Letter we assess the accuracy of the LSDA in describing the magnetic and structural ordering in 3d transition metals, based on total-energy calculations for fcc and bcc iron as a function of volume and type of magnetic order.

A comprehensive study of the ground-state properties of metals, including 3d ferromagnetic metals, has been reported by Moruzzi, Janak, and Williams<sup>1</sup> using the Korringa-Kohn-Rostoker (KKR) method with a LSDA exchange-correlation potential. Kübler<sup>2</sup> subsequently used the augmented-spherical-wave (ASW) method to calculate the total energies of nonmagnetic (NM), ferromagnetic (FM), and antiferromagnetic (AFM) states for both bcc and fcc phases of iron for a range of atomic volumes near equilibrium. The FM state was found to have the lowest energy in the bcc case while the AFM state is the lowest in the fcc case. Surprisingly, the latter was calculated by Kübler to lie 1184 K lower in energy than the former, which is the actual observed ground state of iron at zero temperature. The muffin-tin (MT) approximation, used in the ASW calculations, was suspected to be the most likely

cause of the discrepancy.

To investigate this point further, use has been made of a self-consistent linearized-augmented-plane-wave (LAPW) method<sup>3</sup> which is free from any shape approximations to the potential and charge density. The method has been tested and found to work well on a variety of different systems. Specifically, we have studied the NM and FM phases of both bcc and fcc iron, as well as an AFM fcc phase which consists of alternating layers of up and down spins normal to the [001] direction. What is done for the first time here is to obtain a more accurate estimate of the crystal structure difference in the total energy of iron which, in the past, has been limited by the use of the MT approximation.

We have found the fcc phase more favorable among the two NM states, which is consistent with the fact that Ru, the 4d counterpart of Fe, is hcp. In the bcc case our results give the normal FM state as 3334 K lower in energy, 6.7% larger in equilibrium volume, and 15% smaller in bulk modulus than the NM bcc state. In the fcc case, we find two metastable FM states, with the ground state being either AFM or NM (the two are degenerate within our numerical accuracy). Most notably, the AFM or NM fcc phase has the lowest energy (867 K lower in energy than the FM bcc phase). We believe the failure to predict the proper ground state of iron indicates a fundamental difficulty in the LSDA for describing the magnetic interaction in 3d transition metals.

Before discussing our results further, we summarize the salient points regarding the theoretical and numerical approaches we have used. The LAPW calculations closely follow the methods discussed in Ref. 3 with the

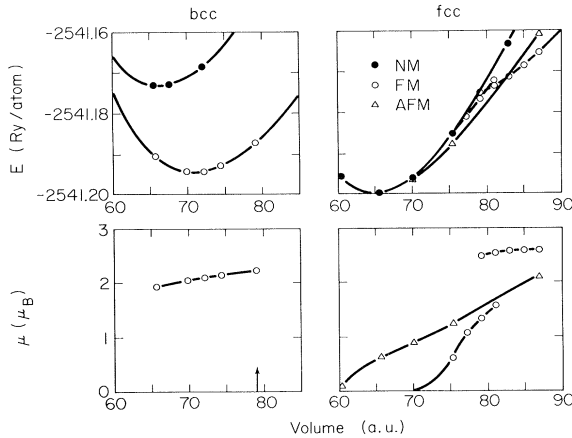


FIG. 1. Total energy per atom ( $E$ ) and magnetic moment ( $\mu$ ) of nonmagnetic (NM), ferromagnetic (FM), and anti-ferromagnetic (AFM) states of bcc and fcc iron.

iron-core states treated self-consistently with use of the full Dirac equation for the spherical part of the potential and the valence electrons treated in the semi-relativistic approximation which neglects spin-orbit coupling. The self-consistent charge densities were evaluated by a histogram sampling of 40, 60, and 30 special  $\mathbf{k}$  points in the irreducible Brillouin zone for the bcc, fcc, and AFM fcc phases, respectively, with an artificial temperature broadening of 2 mRy. All non-spherical and non-MT corrections to the charge density and potential were explicitly included in the self-consistent iterations. Careful tests of the sensitivity of the total energy to basis set size and to the choice of the LAPW energy parameters were performed. Overall, the structure differences of our total energies have an absolute error of less than 1 mRy.

For the LSDA exchange-correlation potential we used the parametrization of Vosko and co-workers<sup>4</sup> which is generally believed to be the most vigorous and accurate. This potential interpolates between the well known high- and low-density limits, using the exact Monte Carlo calculations of Ceperley and Alder<sup>5</sup> at

intermediate densities for both the NM and completely polarized electron gases. For intermediate spin polarization, however, the spin-dependent part of the potential is scaled according to the random-phase approximation.

The total energy per atom calculated for the bcc and fcc phases is shown in Fig. 1 together with the atomic moments. The solid lines are obtained from least-squares fits to the Murnaghan equation of state<sup>6</sup> from which one can determine the equilibrium lattice constants and bulk moduli. They are given in Table I. For FM bcc iron, our calculated equilibrium lattice constant, 5.212 a.u., and bulk modulus, 2.66 Mbar, are in good agreement with recent independent calculations of Hathaway, Jansen, and Freeman.<sup>7</sup> The corresponding experimental values are 5.406 a.u. and 1.68 Mbar, respectively. The discrepancy between theory and experiment is larger than what is typically found for nonmagnetic materials.

The band theory of ferromagnetism is now well understood. The magnetic interaction leads to a spin splitting of the  $d$  bands and a filling of the less bonding majority-spin orbitals at the expense of the more bonding minority-spin orbitals. This causes the volume to increase, which in turn reduces the compression the  $sp$  electron feel (i.e., reduces their kinetic energy), and hence the bulk modulus. Ferromagnetism is established if the Stoner criterion is realized. The NM density of states at the Fermi energy must be reasonably high so that the gain in the kinetic energy is more than compensated for by the loss in the exchange energy. The above conditions are satisfied in the bcc phase. We found that ferromagnetism lowered the total energy by 3334 K, accompanied by an expansion in volume (6.7%) and a reduction in the bulk modulus (15%). This energy difference should not be confused with the Curie temperature ( $T_C = 1041$  K) which is the temperature above which the *average* magnetization vanishes. Over this temperature range the thermodynamics is dominated by spin-wave-like excitations (changes in the direction of

TABLE I. Total energy per atom ( $E$ ) at equilibrium lattice constant ( $a$ ), bulk modulus ( $B$ ), and atomic magnetic moment ( $\mu$ ) of NM, FM, and AFM states of bcc and fcc Fe.

		$E$	$a$ (a.u.)	$B$ (Mbar)	$\mu$ ( $\mu_B$ )
bcc	NM	-2541.173	5.10	3.14	...
	FM	-2541.194	5.21	2.66	2.08
fcc	NM	-2541.200	6.38	3.44	...
	AFM	-2541.200	6.38	3.23	0.64
	FM <sub>1</sub>	-2541.200	6.37	3.90	0.00
	FM <sub>2</sub> <sup>a</sup>	-2541.175	6.81	...	2.47

<sup>a</sup>There is no equilibrium solution for the high-spin state of fcc FM<sub>2</sub> iron in the sense that there is no volume for which the pressure vanishes.

the exchange fields) rather than Stoner-type excitations (changes in the magnitudes of the exchange fields).<sup>8</sup> Thus, substantial local moments persist even above  $T_C$  in contrast to the NM states that we have considered. This is supported by many experiments including the exchange splitting close to  $T_C$  observed in photoemission.<sup>9</sup>

At normal pressure, experiment indicates that the bcc phase of iron is stable below 1183 K ( $\alpha$  phase) and above 1663 K, up to the melting point of 1807 K ( $\delta$  phase). Between 1183 and 1663 K, the fcc  $\gamma$  phase is stable but the temperature is too high for long-range magnetic ordering to occur. Therefore, the magnetic properties of  $\gamma$ -Fe at low temperatures are not well understood.

Early measurements on the fcc Fe alloys,<sup>10</sup> and small particles of fcc-Fe precipitates from supersaturated Cu-Fe solid solutions,<sup>11</sup> led to the conclusion that the ground state of fcc iron is AFM. However, more recent measurements of small-particle precipitates from Cu-Au alloys indicate FM.<sup>12</sup> In addition, films of fcc iron grown on copper surfaces may be either FM or AFM, depending on the crystallographic surface on which the growth occurs.<sup>13</sup> Recent neutron measurements on bulk  $\gamma$ -Fe at high temperature indicate the presence of FM correlations and a substantial local moment.<sup>14</sup>

At normal pressure our results shown in Fig. 1 indicate that the NM and AFM phases of fcc Fe are essentially degenerate. This near-degeneracy is consistent with the low Néel temperature observed in fcc Fe alloys, but is in contrast to Kübler's calculation which placed AFM fcc Fe 1183 K lower in energy than NM fcc Fe. Our results are supported by the fact that our calculations show that the total energy of AFM fcc Fe converges to that of the NM fcc Fe when the atomic moment vanishes. Unlike the FM-NM transition in bcc Fe, there is very little change in the equilibrium volume and bulk modulus between AFM and NM states of the fcc iron. This may be due in part to the small atomic moments ( $0.64\mu_B$ ) in the AFM fcc Fe compared to that of the FM bcc Fe ( $2.08\mu_B$ ). The small differences in the atomic moments from previous calculations<sup>1, 2, 15-17</sup> may reflect (1) different lattice constants, (2) different choices of exchange-correlation potentials, (3) semirelativistic effects which tend to lower the  $sp$  states relative to the  $d$  bands, and (4) the use of the MT approximation in some cases.

In good agreement with earlier calculations,<sup>2, 16</sup> our total energy as a function of atomic volume for FM fcc Fe exhibits two local minima, with the magnetic moment increasing abruptly between them. Thus, our results support the idea the FM fcc Fe can exist in two states with only slightly different energies: a low-volume, low-spin, large-bulk-modulus state, and a high-volume, high-spin, small-bulk-modulus state.

The coexistence of two spin states in FM fcc Fe has long been postulated to explain the Invar anomalies. The origins of the two spin states has been discussed in terms of features of the density of states,<sup>16, 18</sup> while Bagayoko and Callaway<sup>15</sup> have identified the abrupt transition with the occupancy of a nearly flat portion of the  $d$  bands and the disappearance of the corresponding Fermi surface.

Our results can also resolve a small discrepancy regarding the transition from the low-spin state to the high-spin state: Kübler<sup>2</sup> found the transition between  $r_s = 2.64$  and  $2.65$  a.u. and a moment of  $1\mu_B$  while Bagayoko and Callaway<sup>15</sup> reported a larger value of  $r_s(2.71)$  and moment ( $1.52\mu_B$ ). We found metastable solutions for *both* high- and low-spin states between  $r_s = 2.66$  and  $2.68$  a.u. In the low-spin phase, the corresponding atomic moments increase sharply from  $1.35\mu_B$  to  $1.56\mu_B$ . The possibility of more than one solution in a self-consistent calculation was first discovered by Janak<sup>19</sup> in ferromagnetic cobalt.

As can be seen in Fig. 1, the atomic moment decreases with decreasing volume, which indicates that there is a transition back to the NM state as the volume shrinks, the band width increases, and the electrons become delocalized. On the high-volume side, there is another transition in fcc Fe from AFM to the high-spin state of FM near  $r_s = 2.69$  a.u. This is consistent with the experimental observations that fcc-Fe precipitates in Cu ( $r_s = 2.67$ ) are AFM<sup>11</sup> and fcc-Fe precipitates in Cu-Au alloys ( $r_s = 2.78$ ) are FM.<sup>12</sup>

The major result of the present study is that both NM and AFM fcc Fe lie lower in energy than does FM bcc Fe by 867 K. This emphasizes a shortcoming of LSDA in incorrectly describing the effect of the Hund's-rule correlations that are responsible for the formation of atomiclike local moments. Within LSDA, the exchange and correlation potentials are determined *locally* on the basis of the results of a *homogeneous* electron gas of the same spin density at that point. The determination of these local potentials makes no distinction as to whether the spins of the nearest-neighbor atoms are parallel or antiparallel and, therefore, some of the correlations between local moments on different sites are neglected. It is possible that the  $3d$  electrons in iron are localized enough for this effect to become important. Recently, one of us<sup>20</sup> has studied the effects of a nonlocal exchange potential and found a sizable correction to the exchange splitting in nickel. Similar attempts in iron, however, failed because the correction is again large in spite of the good agreement between the uncorrected LSDA energy bands and experiments. These results may be an indication of substantial cancellation between non-local exchange and nonlocal correlation corrections, which must be treated on an equal footing. Hopefully,

the present Letter will stimulate more work along these directions.

This work is supported in part by the Office of Naval Research under Contract No. N00014-79-WR-90028, and in part by the National Science Foundation under Grants No. DMR 82-13768 and No. DMR 81-20550. Use of the computer facilities at the University of Maryland is gratefully acknowledged.

---

<sup>1</sup>V. L. Moruzzi, J. F. Janak, and A. R. Williams, *Calculated Electronic Properties of Metals* (Pergamon, New York, 1978).

<sup>2</sup>J. Kübler, Phys. Lett. **81A**, 81 (1981).

<sup>3</sup>O. K. Andersen, Phys. Rev. B **12**, 3060 (1975); D. D. Koelling and G. O. Arbman, J. Phys. F **5**, 2041 (1975); E. Wimmer, H. Krakauer, M. Weinert, and A. J. Freeman, Phys. Rev. B **24**, 864 (1981); D. R. Hamann, Phys. Rev. Lett. **42**, 662 (1979); S. H. Wei and H. Krakauer, to be published.

<sup>4</sup>S. H. Vosko, L. Wilk, and M. Nusair, Can. J. Phys. **58**, 1200 (1980); S. H. Vosko and L. Wilk, Phys. Rev. B **22**, 3812 (1980).

<sup>5</sup>D. M. Ceperley and B. J. Alder, Phys. Rev. Lett. **45**, 566 (1980).

<sup>6</sup>F. D. Murnaghan, Proc. Nat. Acad. Sci. U.S.A. **3**, 244 (1944).

<sup>7</sup>K. B. Hathaway, H. J. F. Jansen, and A. J. Freeman, Bull. Am. Phys. Soc. **29**, 277 (1984).

<sup>8</sup>C. S. Wang, R. E. Prange, and V. Korenman, Phys. Rev. B **25**, 5766 (1982), and the references therein.

<sup>9</sup>E. Kisker, K. Schroder, M. Campagan, and W. Gudat, Phys. Rev. Lett. **52**, 2285 (1984).

<sup>10</sup>E. I. Kondorskii and V. L. Sedov, Zh. Eksp. Teor. Fiz. **35**, 1579 (1959) [Sov. Phys. JETP **8**, 1104 (1959)].

<sup>11</sup>C. Abrahams, L. Guttman, and J. S. Kasper, Phys. Rev. **127**, 2052 (1962); G. Johanson, M. B. McGirr, and D. A. Wheeler, Phys. Rev. B **1**, 3208 (1970).

<sup>12</sup>U. Gonser, K. Krischel, and S. Nasu, J. Magn. Magn. Mater. **15-18**, 1145 (1980).

<sup>13</sup>J. Wright, Philos. Mag. **24**, 217 (1971); U. Gradmann, W. Kummerle, and P. Tillmans, Thin Solid Films **34**, 249 (1976); W. Keune, R. Halbauer, U. Gonser, J. Lauer, and D. L. Williamson, J. Appl. Phys. **48**, 2976 (1977); U. Gradmann and H. O. Isbert, J. Magn. Magn. Mater. **15-18**, 1109 (1980).

<sup>14</sup>P. J. Brown, H. Capellman, J. Deportes, D. Givord, and K. R. A. Ziebeck, J. Magn. Magn. Mater. **31-34**, 295 (1983).

<sup>15</sup>J. Callaway and C. S. Wang, Phys. Rev. B **16**, 2095 (1977); D. Bagayoko and J. Callaway, Phys. Rev. B **28**, 5419 (1983).

<sup>16</sup>U. K. Poulsen, J. Kollar, and O. K. Andersen, J. Phys. F **6**, L241 (1976); O. K. Andersen, J. Madsen, U. K. Poulsen, D. Jepsen, and J. Kollar, Physica (Utrecht) **86-88B**, 249 (1977).

<sup>17</sup>W. B. Johnson, J. R. Anderson, and D. A. Papaconstantopoulos, Phys. Rev. B **29**, 5337 (1984).

<sup>18</sup>D. M. Roy and D. G. Pettifor, J. Phys. F **7**, L183 (1977).

<sup>19</sup>J. F. Janak, Solid State Commun. **25**, 53 (1978).

<sup>20</sup>C. S. Wang, J. Magn. Magn. Mater. **31-34**, 95 (1983).

## Gradient-Corrected Density Functional Calculation of Elastic Constants of Fe, Co and Ni in bcc, fcc and hcp Structures

G. Y. Guo and H. H. Wang

*Department of Physics, National Taiwan University,  
Taipei, Taiwan 106, R.O.C.*

(Received January 13, 2000)

Systematic *ab initio* calculations of lattice constants, elastic constants and magnetic moments of Fe, Co and Ni in bcc, fcc and hcp structures have been carried out, in part to understand the phase stability and magnetic properties of artificial Fe, Co and Ni structures. The calculations are based on the local spin-density functional theory with generalized gradient corrections (GGA) which are found to describe the properties of these materials rather well. In particular, the calculated lattice constants and bulk modulus of the observed structures are in good agreement with experiments. Also, the theoretical elastic constants agree with the measurements within the numerical uncertainties. Interestingly, several energetically metastable structures are found to be elastically unstable. It is predicted that magnetism has a pronounced influence on both the size and sign of some elastic constants, and hence on the structural stabilities. For example, while both nonmagnetic Fe fcc and hcp structures are metastable phases, ferromagnetic Fe fcc and hcp structures are not. These results would help to gain insight into the formation of certain artificial thin films and superlattices.

PACS. 62.20.Dc – Elasticity, elastic constants.

PACS. 71.15.Mb – Density functional theory, local density approximation.

PACS. 75.20.En – Metals and alloys.

### I. Introduction

The recent advent of advanced thin film growth techniques has stimulated enormous interest in making artificial crystalline structures that do not exist in nature [1-3]. These artificial systems would allow one to better understand the growth mechanism and structural phase transition and also to explore novel physical properties distinct from that of the natural crystals. Well-known artificial structures include fcc Fe on Cu [1], bcc Co on GaAs [2] and bcc Ni on Fe [3]. Stimulated by these interesting experiments, we have performed systematic first-principles density functional total energy calculations of Fe, Co and Ni in three common structures, namely, bcc, fcc and hcp, in both ferromagnetic and nonmagnetic states.

The purpose of this work is multiple. Firstly, density functional theory (DFT) with the local density approximation (LDA) [4] has been used for first-principles studies of the physical properties of a variety of materials. It provides an accurate theoretical estimate of static structural properties, phonon spectra, crystal stability, and pressure-induced phase transformations in many solids [5]. However, there were also problems in the LDA. Notably, it predicted a wrong ground state for iron [7, 8] and certain alkali metals [9]. There has been some considerable effort

worldwide in recent years to improve and go beyond the LDA [5]. In particular, the so-called generalized gradient corrections (GGA) to the LDA have been developed by several groups (see, e.g., [10] and references therein). These GGA calculations have been found to considerably improve the LDA results in many cases [11]. For example, the GGA calculations predict a correct ground state structure for iron and also substantially reduce the discrepancy in e.g., lattice constants between the theory and experiments [11]. However, a stringent test of the GGA is to calculate the elastic constants of, e.g., 3d magnetic metals. Therefore, we have performed systematic DFT-LDA-GGA calculations of elastic constants of Fe, Co and Ni in their observed structures.

Secondly, the density functional total energy of Fe, Co and Ni in a number of structures has been calculated by several groups in the past (e.g., [12]). There is always a minimum in the total energy vs volume curve for every structure considered [12]. However, this does not necessarily mean that these phases are a stable or metastable structure. They could be unstable if at least one of their elastic constants is negative. A good example of elastic instability is bcc Co [13]. Clearly, to better understand the phase stability of the artificial structures, one needs to know the elastic constants of these structures. We thus have calculated the elastic constants of Fe, Co and Ni in their most common bcc, fcc and hcp structures. Note that almost all transition metal artificial magnetic thin films and superlattices contain at least one of these three elements.

Thirdly, since the GGA calculations describe satisfactorily lattice and elastic constants of Fe, Co and Ni in their observed structures, as will be shown below, the GGA predictions for the structural properties of the hitherto unobserved structures are expected to be rather reliable. Therefore, one may be able to use the calculated lattice constants and the signs of calculated elastic constants to help fabricate new artificial structures.

The organization of the rest of this paper is as follows. In the next section, we describe briefly the relevant elastic theory and the determination of the elastic constants of cubic and hexagonal systems via first-principles total energy calculations. Also the computational details will be given. In Sec. III, we present the calculated total energies, lattice constants and bulk moduli. In Sec. IV, we report the calculated elastic constants. In Sec. V, we will discuss the effects of magnetism on the phase stability of Fe, Co and Ni. A short summary is also given in this section.

## II. Elastic theory and computational details

For small strains ( $\underline{\epsilon}$ ) on a solid, the Hook's law is applicable and the elastic energy  $E_e$  is approximately a quadratic function of the strain components

$$E_e(V_0, \underline{\epsilon}) = V_0 \sum_{i,j=1}^6 \frac{1}{2} C_{ij} e_i e_j \quad (1)$$

where  $C_{ij}$  are the elastic constants,  $V_0$  is the total volume and  $e_i$  are the components of the strain tensor

$$\underline{\epsilon} = \begin{pmatrix} e_1 & e_6 & e_5 \\ e_6 & e_2 & e_4 \\ e_5 & e_4 & e_3 \end{pmatrix} \quad (2)$$

in conventional elastic theory notation [14]. Under these strains, the original lattice vectors  $\mathbf{a}$  would be transformed into the strained ones  $\mathbf{a}'$  as  $\mathbf{a}' = (I + \underline{\epsilon})\mathbf{a}$  where  $I$  is the identity matrix.

For a cubic crystal, there are only three independent elastic constants, namely,  $C_{11}$ ,  $C_{12}$  and  $C_{44}$ . Furthermore, the bulk modulus  $B$  and tetragonal shear constant  $C'$  are related to  $C_{11}$  and  $C_{12}$ , i.e.,  $B = \frac{1}{3}(C_{11} + 2C_{12})$ ,  $C' = \frac{1}{2}(C_{11} - C_{12})$ .  $C_{44}$  is the trigonal shear constant.  $B = V \frac{d^2 E}{dV^2}$  can be determined by fitting the calculated total energy  $E$  as a function of volume  $V$  to the equation of state of Murnaghan [15].  $C'$  ( $C_{44}$ ) may be determined by a polynomial fitting of the calculated total energy  $E$  as a function of the tetragonal (orthorhombic) strain

$$\underline{\epsilon} = \begin{pmatrix} \varepsilon & 0 & 0 \\ 0 & \varepsilon & 0 \\ 0 & 0 & -\frac{\varepsilon(2+\varepsilon)}{(1+\varepsilon)^2} \end{pmatrix} (\underline{\epsilon} = \begin{pmatrix} 0 & \varepsilon & 0 \\ \varepsilon & 0 & 0 \\ 0 & 0 & \frac{\varepsilon^2}{1+\varepsilon^2} \end{pmatrix}). \quad (3)$$

The associated energy change due to the strain is approximately given by

$$\Delta E(V_0) = \frac{3}{2V_0} C' \varepsilon^2 (\Delta E(V_0) = 2V_0 C_{44} \varepsilon^2). \quad (4)$$

For a hexagonal solid, there are five independent elastic constants, namely,  $C_{11}$ ,  $C_{12}$ ,  $C_{13}$ ,  $C_{33}$  and  $C_{55}$ . Total energy calculation of the elastic constants of a hcp solid is rather involved. Indeed, the elastic constants of only a few elemental hcp metals have been calculated [16]. The five elastic constants of a hcp solid are related to the bulk modulus ( $B$ ) and four shear constants ( $C_{11} + C_{12}$ ,  $C_{11} - C_{12}$ ,  $\frac{1}{2}C_{33}$  and  $2C_{55}$ ) [16]. The  $B$  can be written as

$$B = \frac{2}{9} \left( C_{11} + C_{12} + 2C_{13} + \frac{1}{2}C_{33} \right). \quad (5)$$

Here, we determine the four shear constants (hence the elastic constants) by a polynomial fitting of the calculated total energy as a function of the shear strains, as described in Ref [16]. The shear constants ( $C_{11} + C_{12}$ ) and  $C_{33}$  correspond to the uniform in-plane strain and the interlayer strain with the strain matrice

$$\begin{pmatrix} \varepsilon & 0 & 0 \\ 0 & \varepsilon & 0 \\ 0 & 0 & 0 \end{pmatrix} \quad (6)$$

and

$$\begin{pmatrix} 0 & 0 & 0 \\ 0 & 0 & 0 \\ 0 & 0 & \varepsilon \end{pmatrix} \quad (7)$$

respectively. The associated energy changes are given, respectively, by

$$\Delta E(V_0) = V_0(C_{11} + C_{12})\varepsilon^2 \quad (8)$$

and

$$\Delta E(V_0) = \frac{1}{2} V_0 C_{33} \varepsilon^2. \quad (9)$$

The shear constant ( $C_{11} - C_{12}$ ) was calculated by introducing a monoclinic distortion with the strain matrix

$$\begin{pmatrix} +\varepsilon & 0 & 0 \\ 0 & -\varepsilon & 0 \\ 0 & 0 & 0 \end{pmatrix}. \quad (10)$$

The associated energy change is given by

$$\Delta E(V_0) = V_0(C_{11} - C_{12})\varepsilon^2. \quad (11)$$

This distortion increases the  $x$  axis and decreases the  $y$  axis. The shear constant  $C_{55}$  was calculated by introducing a triclinic distortion with the strain matrix

$$\begin{pmatrix} 0 & 0 & \varepsilon \\ 0 & 0 & 0 \\ \varepsilon & 0 & 0 \end{pmatrix} \quad (12)$$

and the associated energy change is given by

$$\Delta E(V_0) = 2V_0C_{55}\varepsilon^2. \quad (13)$$

We have used the highly accurate all-electron full-potential linear augmented plane wave (FLAPW) method [17] to calculate the total energies and magnetic properties of Fe, Co and Ni. The calculations are based on the first-principles density functional theory with the standard local density approximation (LDA) to the exchange-correlation potential [18]. The latest generalized gradient corrections (GGA) of Perdew-Burke-Ernzerhof [10] have been included in all the calculations. The muffin-tin radius used is 2.2 atomic units (a.u.). Fe  $1s$ ,  $2s$  and  $2p$  are treated as core states,  $3d, 4s$  and  $4p$  as band states and the shallow core states  $3s$  and  $3p$  are also treated as band states by using the so-called local orbitals [17]. For Co and Ni,  $3s$  state is also treated as a core state. Inside the muffin-tin spheres, the wavefunctions, charge densities, and potential are expanded in terms of the spherical harmonics. The cut-off angular momentum ( $L_{max}$ ) is 10 for the wave functions and 4 for charge densities (potentials). The Brillouin zone integration is carried out by using the improved tetrahedron method [19]. The number of the augmented plane waves included is about 90 per atom, i.e.,  $R_{mt}K_{max} = 9$  [17]. The numbers of the  $k$ -points in the irreducible Brillouin zone wedge (IBZW) for nonmagnetic and ferromagnetic bcc, fcc and hcp are, respectively, 104, 72, 120. The self-consistent cycles are terminated when the total energy converges to within 0.01 mRy/atom. In the shear constant calculations, the crystal is elastically deformed and may have a lower symmetry. Furthermore, the total energy change due to a shear strain is often very small (a few tenths of mRy/atom). Thus, more  $k$ -points in the IBZW are used. For example, when calculating hcp  $C_{55}$ , we used about 900  $k$ -points. The self-consistent cycles are terminated when the total energy converges to within 0.002 mRy/atom.



### III. Total energy and lattice constants

#### III-1. Iron

The calculated total energy as a function of volume per atom for bcc, fcc and hcp Fe is displayed in Fig. 1. Both the nonmagnetic and ferromagnetic states are considered. For the total energies of the hcp structure in Fig. 1, the theoretical  $c/a$  ratios of 1.73 and 1.59 have been used for the ferromagnetic and nonmagnetic cases, respectively. The  $c/a$  ratio was determined as follows. In each case, the  $c/a$  ratio was initially fixed at the ideal value of 1.63 while the total energy was calculated for different volumes. The volume was then fixed at the minimal energy one while the total energy was calculated for different  $c/a$  ratios to find the minimal energy  $c/a$ . This procedure was repeated till we found the change in the  $c/a$  to be within 1 %. The theoretical  $c/a$  ratio for the nonmagnetic phase is in good agreement with the previous GGA calculations [20, 21]. Each total energy vs volume per atom was fitted to the equation of state of Murnaghan [15] to obtain the theoretical lattice constant, bulk modulus and minimal total energy. The results are listed in Table I. Fig. 1 shows that the ferromagnetic bcc structure is the ground state for Fe, in agreement with the experiments and also with the previous GGA calculations [11]. The calculated bcc lattice constant  $a$  is only 1 % smaller than the experimental value (Table I). The calculated bulk modulus  $B$  is also in satisfactory agreement with experiments (Table I). Fig. 1 indicates that under pressure, ferromagnetic bcc Fe would first transform to nonmagnetic hcp structure. The theoretical transition pressure is estimated to be 121 kbar, be rather close to the value of 130 kbar determined experimentally [22]. Furthermore, the theoretical  $c/a$  ratio of 1.59 is close to the experimental values in the pressure range of 150 ~ 3000 kbar [22, 23]. In contrast, the LDA calculations [7, 8] predicted a wrong ground state (non-magnetic fcc), the ferromagnetic bcc lattice constant being 4 % too small and the bulk modulus of the ferromagnetic bcc structure being 50 % too large. In short, the present LDA-GGA calculations not only give a correct

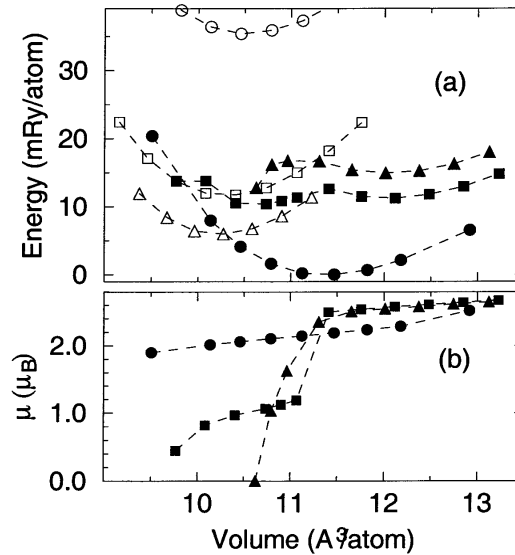


FIG. 1. (a) Total energy (relative to -2545.611 Ry/atom) of Fe as a function of volume per atom for bcc (circles), fcc (squares) and hcp (triangles). The curves are a polynomial fit to the total energies. Solid symbols denote the ferromagnetic states and open symbols, the nonmagnetic states. (b) Magnetic moment ( $\mu$ ) of bcc, fcc and hcp Fe as a function of volume per atom.

TABLE I. The theoretical and experimental lattice constant ( $a_0$ ), atomic volume ( $V_0$ ), elastic constants, magnetic moment  $m_s$  and total energy ( $E_0$ ) of bcc, fcc and hcp Fe. Both nonmagnetic (NM) and ferromagnetic (FM) results are listed. The total energy of NM and FM hcp Fe is, respectively, -2545.6047 and -2545.5958 Ry/atom. The experimental values for the ferromagnetic bcc Fe (Exp<sup>a</sup>) [14] and for the nonmagnetic hcp Fe at 500 kbar (Exp<sup>b</sup>) [22] are also listed for comparison.

(a)

bcc Fe	$a_0$	$V_0$	$B$	$C'$	$C_{11}$	$C_{12}$	$C_{44}$	$m_s$	$E_0$
	Å	Å <sup>3</sup> /atom	Mbar	Mbar	Mbar	Mbar	Mbar	$\mu_B$	Ry/atom
FM	2.84	11.40	1.86	0.69	2.79	1.40	0.99	2.17	-2545.6107
Exp <sup>a</sup>	2.87	11.82	1.72	0.48	2.32	1.36	1.17	2.22	
NM	2.76	10.52	2.76	-1.10	1.30	3.49	1.41		-2545.5754

(b)

fcc Fe	$a_0$	$V_0$	$B$	$C'$	$C_{11}$	$C_{12}$	$C_{44}$	$m_s$	$E_0$
	Å	Å <sup>3</sup> /atom	Mbar	Mbar	Mbar	Mbar	Mbar	$\mu_B$	Ry/atom
FM	3.63	11.97	1.82	-0.77	0.79	2.33	0.23	2.55	-2545.5902
NM	3.45	10.30	3.17	1.25	4.84	2.34	2.87		-2545.5908

(c)

hcp	$a_0$	$c/a$	$V_0$	$B$	$C_{11}+C_{12}$	$C_{11}-C_{12}$	$C_{11}$	$C_{12}$	$C_{13}$	$C_{33}$	$C_{55}$	$m_s$
Fe	Å		Å <sup>3</sup> /atom	Mbar	Mbar	Mbar	Mbar	Mbar	Mbar	Mbar	Mbar	$\mu_B$
FM	2.52	1.732	12.04	1.56	4.17	-0.29	1.94	2.23	0.87	3.14	-0.62	2.54
NM	2.46	1.586	10.23	2.97	7.27	3.85	5.56	1.71	1.43	6.47	2.48	
Exp <sup>b</sup>			8.89		9.40	3.40	6.40	3.00	2.55	6.50	4.20	

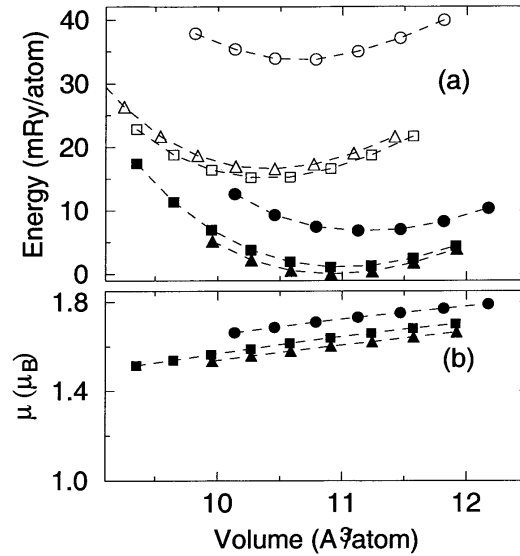


FIG. 2. (a) Total energy (relative to  $-2786.956 \text{ Ry/atom}$ ) of Co as a function of volume per atom for hcp (triangles), fcc (squares) and bcc (circles). The curves are a polynomial fit to the total energies. Solid symbols denote the ferromagnetic states and open symbols, the nonmagnetic states. (b) Magnetic moment ( $\mu$ ) of hcp, fcc and bcc Co as a function of volume per atom.

ground state structure of Fe but also describe accurately the lattice constant and structural transformations under pressure.

The calculated spin magnetic moments for the ferromagnetic bcc, fcc and hcp are also shown in Fig. 1 as a function of volume per atom. Interestingly, the magnetic moments of both close-packed structures changes dramatically with volume when the volume is less than  $11.5 \text{ \AA}^3/\text{atom}$ . For example, the magnetic moment of fcc phase clapses completely at  $10.6 \text{ \AA}^3/\text{atom}$  whilst at  $11.5 \text{ \AA}^3/\text{atom}$  it is as large as  $2.5 \mu_B$ . In contrast, the magnetic moment of bcc Fe decreases monotonically and slowly as the volume is compressed. Nonetheless, these interesting behaviors of the magnetic moments of the close-packed structures of Fe have been elaborated already in several previous papers [24, 25]. Thus they will not be discussed further in this paper except that the calculated spin magnetic moment of the bcc phase agrees well with the experiments (Table I).

### III-2. Cobalt

The calculated total energy and spin magnetic moment as a function of volume per atom for hcp, fcc and bcc Co is displayed in Fig. 2. Both the nonmagnetic and ferromagnetic states are considered. For the total energies of the hcp structure in Fig. 2, the theoretical  $c/a$  ratio of 1.62 has been used for both the ferromagnetic and nonmagnetic states. The theoretical lattice constant, bulk modulus and minimal total energy determined from these total energy vs volume curves are listed in Table II. Fig. 2 shows that the ferromagnetic hcp structure is the ground state for Co, in agreement with the experiments [14]. However, the total energy vs volume of ferromagnetic fcc Co lies immediately above the hcp phase, the energy difference between these two phases is only

TABLE II. The theoretical and experimental lattice constant ( $a_0$ ), atomic volume ( $V_0$ ), elastic constants, magnetic moment ( $m_s$ ), total energy ( $E_0$ ) of hcp, fcc and bcc Co. Both the nonmagnetic (NM) and ferromagnetic (FM) results are listed. The total energy of NM and FM hcp Co is, respectively, -2786.9397 and -2786.9563 Ry/atom. The experimental values for ferromagnetic hcp Co (Exp<sup>a</sup>) [14, 26] and ferromagnetic fcc Co (Exp<sup>b</sup>) [27] are also listed for comparison.

(a)

hcp	$a_0$	$c/a$	$V_0$	$B$	$C_{11}+C_{12}$	$C_{11}-C_{12}$	$C_{11}$	$C_{12}$	$C_{13}$	$C_{33}$	$C_{55}$	$m_s$
Co	Å		Å <sup>3</sup> /atom	Mbar	Mbar	Mbar	Mbar	Mbar	Mbar	Mbar	Mbar	$\mu_B$
FM	2.50	1.62	10.92	2.21	5.41	1.65	3.53	1.88	1.16	4.43	0.63	1.60
Exp <sup>b</sup>	2.51	1.62	11.09	1.91	4.72	1.42	3.07	1.65	1.03	3.58	0.76	1.58
NM	2.45	1.62	10.41	2.62	6.30	4.54	5.42	0.88	2.51	1.68	1.29	

(b)

fcc Co	$a_0$	$V_0$	$B$	$C'$	$C_{11}$	$C_{12}$	$C_{44}$	$m_s$	$E_0$
	Å	Å <sup>3</sup> /atom	Mbar	Mbar	Mbar	Mbar	Mbar	$\mu_B$	Ry/atom
FM	3.53	10.99	2.16	0.68	3.25	1.89	1.56	1.64	-2786.0552
Exp <sup>a</sup>	3.55	11.14						1.72	
NM	3.46	10.39	2.60	1.22	4.30	1.86	1.80		-2786.9411

(c)

bcc Co	$a_0$	$V_0$	$B$	$C'$	$C_{11}$	$C_{12}$	$C_{44}$	$m_s$	$E_0$
	Å	Å <sup>3</sup> /atom	Mbar	Mbar	Mbar	Mbar	Mbar	$\mu_B$	Ry/atom
FM	2.82	11.18	2.09	-0.24	1.93	2.41	1.31	1.73	-2786.9395
NM	2.77	10.63	2.47	-2.70	-1.16	4.24	3.68		-2786.0225

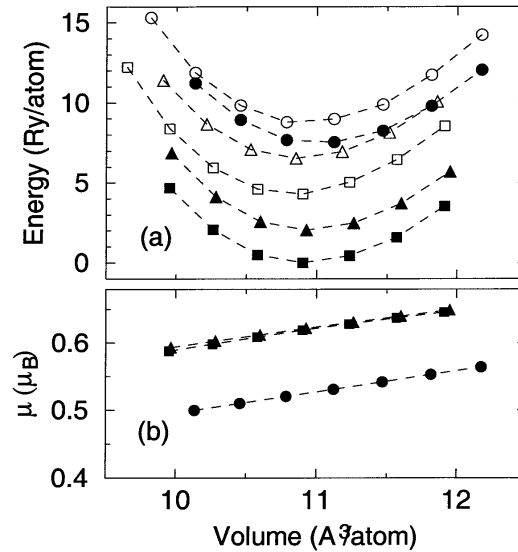


FIG. 3. (a) Total energy (relative to -3041.667 Ry/atom) of Ni as a function of volume per atom for fcc (squares), hcp (triangles), bcc (circles). The curves are a polynomial fit to the total energies. Solid symbols denote the ferromagnetic states and open symbols, the nonmagnetic states. (b) Magnetic moment ( $\mu$ ) of fcc, hcp and bcc Ni as a function of volume per atom.

1 mRy/atom. Furthermore, all the calculated elastic constants are positive (see next section). This explains why the artificial fcc Co films can be grown up to 2000 Å [27]. The calculated hcp and fcc lattice constants differ from the corresponding experimental values only by less than 0.5 % (Table II). The calculated  $B$  is however 15 % larger than the experimental value (Table I). Note that the theoretical bcc Co lattice constant (2.82 Å) is also close to that (2.83 Å) of the artificial Co bcc structure [2]. Unlike iron (Fig. 1), the total energy vs volume phase diagram (Fig. 2) is simple. All the magnetic curves lie below the nonmagnetic ones and show no kink or other anomalies. Furthermore, the calculated magnetic moments for the hcp, fcc and bcc show an expected behavior, i.e., the magnetic moment decreases monotonically with the volume. The bcc structure has a highest magnetic moment at all the volumes considered. The calculated spin magnetic moment at the minimal energy lattice constant for hcp Co is somewhat larger than the experimental one. For fcc Co the calculated and measured spin magnetic moments agree well (Table II).

### III-3. Nickel

The calculated total energy and spin magnetic moment as a function of volume per atom for fcc, hcp and bcc Ni is displayed in Fig. 3. Both the nonmagnetic and ferromagnetic states are considered. For the total energies of the hcp structure in Fig. 3, the theoretical  $c/a$  ratio of 1.65 has been used for the ferromagnetic and nonmagnetic phases. This  $c/a$  value is in good agreement with a very recent calculation [21]. The theoretical lattice constant, bulk modulus and minimal total energy determined from these total energy vs volume curves are listed in Table III.

TABLE III. The theoretical and experimental lattice constant ( $a_0$ ), atomic volume ( $V_0$ ), elastic constants, magnetic moment ( $m_s$ ), and total energy ( $E_0$ ) of bcc, fcc and hcp Ni. Both the nonmagnetic (NM) and ferromagnetic (FM) results are listed. The total energy of NM and FM hcp Ni is, respectively, -3041.6602 and -3041.6647 Ry/atom. The experimental values for the ferromagnetic fcc Ni (Exp) [14] are also listed for comparison.

(a)									
fcc Ni	$a_0$	$V_0$	$B$	$C'$	$C_{11}$	$C_{12}$	$C_{44}$	$m_s$	$E_0$
	Å	Å <sup>3</sup> /atom	Mbar	Mbar	Mbar	Mbar	Mbar	$\mu_B$	Ry/atom
FM	3.52	10.92	1.99	0.66	2.87	1.55	1.50	0.62	-3041.6667
Exp	3.52	11.09	1.86	0.54	2.48	1.55	1.24	0.61	
NM	3.51	10.83	2.07	0.83	3.23	1.62	0.39		-3041.6624

(b)												
hcp	$a_0$	$c/a$	$V_0$	$B$	$C_{11}+C_{12}$	$C_{11}-C_{12}$	$C_{11}$	$C_{12}$	$C_{13}$	$C_{33}$	$C_{55}$	$m_s$
Ni	Å		Å <sup>3</sup> /atom	Mbar	Mbar	Mbar	Mbar	Mbar	Mbar	Mbar	Mbar	$\mu_B$
FM	2.48	1.645	10.93	2.00	4.98	2.89	3.94	1.05	1.30	3.76	1.05	0.62
NM	2.47	1.649	10.87	2.22	4.56	1.79	3.18	1.39	2.28	1.76	1.57	

(c)									
bcc Ni	$a_0$	$V_0$	$B$	$C'$	$C_{11}$	$C_{12}$	$C_{44}$	$m_s$	$E_0$
	Å	Å <sup>3</sup> /atom	Mbar	Mbar	Mbar	Mbar	Mbar	$\mu_B$	Ry/atom
FM	2.80	11.02	1.96	-0.33	1.57	2.23	1.56	0.53	-3041.6592
NM	2.80	10.93	2.04	-0.96	0.84	2.76	3.95		-3041.6579

Fig. 3 shows that the ferromagnetic fcc structure is the ground state for Ni, in agreement with the experiments [14]. Furthermore, the calculated fcc lattice constant  $a$  is only 0.5 % smaller than the experimental value (Table III). The calculated  $B$  is 7 % larger than the experimental value (Table III). Note that artificial hcp Ni<sub>1-x</sub>Fe<sub>x</sub> ( $0 < x < 20\%$ ) films were recently made [28]. The lattice parameters  $a$  of 2.50 Å and  $c$  of 4.07 Å are close to the theoretical values calculated here

(Table III). Unlike iron (Fig. 1), the total energy vs volume phase diagram (Fig. 2) is simple. All the magnetic curves lie below the associated nonmagnetic ones, respectively and show no kink or other anomalies. Furthermore, the calculated magnetic moments for the hcp, fcc and bcc show an expected behavior, i.e., the magnetic moment decreases monotonically with the volume. The calculated and measured spin magnetic moments agree very well. Unlike bcc Co, the bcc Ni has a smallest magnetic moment among the three structures. Furthermore, the magnetization energy of the bcc structure is small and the energy of the ferromagnetic bcc is still above that of the nonmagnetic fcc and hcp phases (Fig. 3).

#### IV. Elastic constants

##### IV-1. Irons

The theoretical shear constants of bcc, fcc and hcp Fe in both ferromagnetic and nonmagnetic states calculated as described in Sec. II, are listed in Table I. All the elastic constants for each of these phases derived from the calculated shear constants and bulk modulus, are listed in table 1. Table I shows that for the ferromagnetic bcc structure, the calculated and measured elastic constants agree within 20 %. This level of the agreement is considered to be satisfactory because, unlike the calculations of lattice constants and bulk modulus, the calculated elastic constants are rather sensitive to the numerical uncertainties and thus much more demanding. Interestingly, some experimental elastic constants of nonmagnetic hcp Fe measured at 500 kbar [22] (also listed in Table I) are close to the calculated values for the same structure.

From Fig. 1, all the six phases appear to be either a stable or metastable phase. As mentioned in Sec. 1, this is not necessarily the case. Table I shows that nonmagnetic bcc, ferromagnetic fcc and hcp Fe are not a metastable state since they are unstable against one shear deformation or another.

##### IV-2. Colbalt

The theoretical shear constants of hcp, fcc and bcc Co in both ferromagnetic and nonmagnetic states calculated as described in Sec. II, are listed in Table II. All the elastic constants for each of these phases derived from the calculated shear constants and bulk modulus, are listed in Table II. Table II shows that for the ferromagnetic hcp structure, the calculated and measured elastic constants agree within up to 25 %. This level of the agreement is again considered to be rather satisfactory because of the reasons mentioned in the previous subsection. Unlike iron, only nonmagnetic and ferromagnetic bcc phases of Co are not a metastable state since they have negative shear constants (Table II). Furthermore,  $C'_{11}$  of the nonmagnetic bcc structure is also negative due to the large negative value of the shear constant  $C'$ .

##### IV-3. Nickel

The theoretical shear constants of fcc, hcp and bcc Ni in both ferromagnetic and nonmagnetic states calculated as described in Sec. II, are listed in Table III. All the elastic constants for each of these phases derived from the calculated shear constants and bulk modulus, are listed in Table III. Table III shows that for the ferromagnetic fcc structure, the calculated and measured elastic constants agree within up to 20 %. This level of the agreement is considered to be satisfactory

because of the reasons mentioned before. Unlike iron but like cobalt, only nonmagnetic and ferromagnetic bcc phases of Co are not a metastable state since they have negative shear constants. Unlike bcc Co,  $C_{11}$  of the nonmagnetic bcc Ni is positive.

## V. Discussion and summary

Remarkably, Tables I-III and Figures 1-3 show that the occurrence of magnetism in a solid not only increases its lattice constant and reduces its bulk modulus (i.e., makes the solid softer) but also affects its structural stability. These magnetic effects are particularly pronounced in iron perhaps because iron has a largest spin moment among the materials studied here. For example, the existence of the ferromagnetism increases the bcc Fe lattice constant by 4 % and reduces the bulk modulus by 45 % (Table I). Furthermore, nonmagnetic bcc Fe has the highest total energy among the phases considered (Fig. 1) and is elastically unstable (i.e.,  $C'$  is negative) (Table I). Ferromagnetism makes the bcc structure to become the ground state for iron and also elastically stable. It appears to be a rule of thumb that magnetism in a solid generally increases its lattice constant and reduces its bulk modulus (see, e.g., Tables I-III). However, this is no general rule as how the magnetism would affect the phase stability and the total energy. For example, in contrast to the bcc Fe structure, the occurrence of the ferromagnetism destabilizes the fcc and hcp Fe structures which have certain negative elastic constants (Table I). The total energy of the nonmagnetic hcp Fe is lower than that of the ferromagnetic hcp Fe (Fig. 1).

Summarizing, we have carried out systematic LDA-GGA calculations of lattice constants, elastic constants and magnetic moments of Fe, Co and Ni in their three most common structures (i.e., bcc, fcc and hcp structures). We find that the GGA of Perdew, Burke and Ernzerhof [10] removes most of the errors found in the previous LDA calculations (e.g., [7, 8]). Notably, the LDA-GGA predicts a correct ground state structure for iron and a pressure-induced transformation from the ferromagnetic bcc to the nonmagnetic hcp structure with a transition pressure being close to the experimental value. Furthermore, the calculated lattice constants for all the three elements are in very good agreement with experiments. It is thus concluded that the LDA-GGA describes well the total energy vs structure phase diagram of the 3d transition metals. Currently, there is considerable interest in growing and studying the physical properties of artificial 3d magnetic thin films and superlattices. The LDA-GGA calculations would therefore help to gain insight into the phase stability, magnetism and other novel properties of these artificial made structures, and to provide some guidance to grow new metastable thin films and superlattices. In this context, the calculation of the minimal energy lattice constants and also elastic constants would be particularly interesting since a metastable structure is usually grown on a substrate with a similar lattice constant. We find that magnetism has pronounced effects on the lattice constant, the phase stability and also the ordering of the total energies of various structures.

The authors acknowledge support from the National Science Council of ROC (NSC 88-2112-M002-0043, NSC 89-2112-M002-0025).

## References

- [ 1 ] W. Keune *et al.*, J. Appl. Phys. **48**, 2976 (1977).
- [ 2 ] G. A. Prinz, Phys. Rev. Lett. **54**, 1051 (1985).



- [ 3 ] B. Heinrich *et al.*, J. Vac. Sci. Technol. **A64**, 1376 (1986).
- [ 4 ] P. Hohenberg and W. Kohn, Phys. Rev. **B136**, 864 (1964); W. Kohn and L.J. Sham, Phys. Rev. **A140**, 1133 (1965).
- [ 5 ] R. O. Jones and O. Gunnarsson, Rev. Mod. Phys. **61**, 689 (1989).
- [ 6 ] A. T. Paxton, M. Methfessel and H. M. Polatoglou, Phys. Rev. **B41**, 8127 (1990).
- [ 7 ] C. S. Wang, B. M. Klein and H. Krakauer, Phys. Rev. Lett. **16**, 1852 (1985).
- [ 8 ] G. Y. Guo *et al.*, Solid State Comm. **79**, 121 (1991).
- [ 9 ] V. L. Sliwko *et al.*, J. Phys.: Condens. Matter **8**, 799 (1996).
- [10] J. P. Perdew, S. Burke and M. Ernzerhof, Phys. Rev. Lett. **77**, (1996) 3865.
- [11] D. J. Singh, W. E. Pickett and H. Krakauer, Phys. Rev. **B43**, 11628 (1991).
- [12] A. T. Paxton, M. Methfessel and H. M. Polatoglou, Phys. Rev. **B41**, 8127 (1990).
- [13] A. Y. Liu and D. J. Singh, Phys. Rev. **B47**, 8515 (1993).
- [14] C. Kittel, *Introduction to Solid State Physics*, 7th ed. (Wiley, New York, 1996).
- [15] F. D. Murnaghan, Proc. Nat. Acad. Sci. U.S.A. **3**, 244 (1944).
- [16] L. Fast *et al.*, Phys. Rev. **B51**, 17431 (1995).
- [17] P. Blaha, K. Schwarz, and J. Luitz, WIEN97, Vienna University of Technology 1997. (Improved and updated Unix version of the original copyrighted WIEN-code, which was published by P. Blaha, K. Schwarz, P. Sorantin, and S.B. Trickey, in Comput. Phys. Commun. 59, 399 1990).
- [18] D. M. Ceperley and B. J. Alder, Phys. Rev. Lett. **45**, 566 (1980).
- [19] P. E. Blöchl, O. Jepsen and O. K. Andersen, Phys. Rev. **B49**, 16223 (1994).
- [20] P. Söderlind, J. A. Moriarty, J. M. Wills, Phys. Rev. **B53**, 14063 (1996).
- [21] J. X. Zheng-Johansson, O. Eriksson and B. Johansson, Phys. Rev. **B59**, 6131 (1999).
- [22] A. P. Jephcoat, H. K. Mao, and P. M. Bell, J. Geophys. Res. **91**, 4677 (1986).
- [23] H. K. Mao *et al.*, J. Geophys. Res. **95**, 21737 (1990).
- [24] V. L. Moruzzi *et al.*, Phys. Rev. **B34**, 1784 (1986).
- [25] P. M. Marcus, V. L. Moruzzi, S.-L. Qiu, Phys. Rev. **B60**, 369 (1999).
- [26] H. J. McSkimin, J. Appl. Phys. **26**, 406 (1955).
- [27] G. Harp *et al.*, Phys. Rev. **B48**, 17538 (1993).
- [28] J.C.A. Huang *et al.*, Phys. Rev. **57**, 11517 (1998).

# Band theory of insulating transition-metal monoxides: Band-structure calculations

K. Terakura and T. Oguchi\*

*Institute for Solid State Physics, University of Tokyo, Roppongi, Minato-ku, Tokyo 106, Japan*

A. R. Williams

*IBM Thomas J. Watson Research Center, P.O. Box 218, Yorktown Heights, New York 10598*

J. Kübler

*Fachgebiet Theoretische Physik, Institut für Festkörperphysik, Hochschulstrasse 2, D-6100 Darmstadt, West Germany*

(Received 11 April 1984)

The electronic structure of the insulating antiferromagnetic transition-metal compounds MnO, FeO, CoO, and NiO, which have been regarded as the prototypes of the concept of a Mott insulator, is discussed with use of energy-band theory based on the local-spin-density treatment of exchange and correlation. It is shown that the band structure is very sensitive to the magnetic ordering and that the ground-state magnetic ordering is special in the sense that it makes the  $e_g$  ( $x^2-y^2$ ,  $3z^2-r^2$ ) band particularly narrow, which is crucial to the insulating nature of NiO. A detailed analysis is made of this particular aspect of the ground-state magnetic ordering. As for FeO and CoO, it is suggested that the population imbalance among the  $t_{2g}$  ( $xy$ ,  $yz$ ,  $zx$ ) orbitals induced by the intra-atomic exchange interaction may cause a gap to open at the Fermi level.

## I. INTRODUCTION

The transition-metal monoxides MnO, FeO, CoO, and NiO, which are all antiferromagnetic insulators, have occupied a special place in condensed-matter physics for a long-time, because the microscopic origin of their insulating nature<sup>1-6</sup> and their inter-atomic magnetic coupling is unclear.<sup>7,8</sup> The common understanding of these problems is that these materials are Mott insulators and that the magnetic coupling is due to super-exchange. Most previous theoretical analyses of the properties of these materials start from the strong correlation limit, i.e.,  $U/W \gg 1$  with  $U$  and  $W$  the intra-atomic Coulomb integral and the width of the valence band, respectively.<sup>2,3,5,6,9</sup> An extensive review on the theories and analysis of experimental data up to 1977 was given by Brandow<sup>3</sup> from this point of view. Kunz and co-workers<sup>4,5</sup> tried to quantify this approach by taking account of correlation effects beyond the Hartree-Fock approximation with the valence-bond approach. The significant results of this calculation are that the unoccupied  $d$  states are separated from the occupied ones by about 10 eV and that the gap between the occupied  $d$  states and the bottom of the conduction band is 4.8 eV. The large energy separation between the occupied and unoccupied  $d$  states is due to the intra-atomic Coulomb interaction and therefore will not be affected by the magnetic ordering. Although some aspects of models characterized by  $U/W \gg 1$  are consistent with several experimental results concerning the optical gap and the insulating nature, some of the recent experimental results<sup>10-13</sup> are not necessarily consistent with the strong-correlation-limit picture. Therefore, it is worthwhile to study the electronic structure of these substances with the self-consistent band-structure theory based on the local-spin-

density-functional method to reexamine the implication of various experimental data.

Wilson<sup>14</sup> was the first to show that MnO and NiO could be band insulators in their ground-state antiferromagnetic ordering, but the result was not sufficiently convincing, because of the lack of the self-consistency in the calculation. An extensive study of the band structures of transition-metal monoxides in the nonmagnetic state was made by Mattheiss.<sup>15,16</sup> A qualitatively important output of the work was the conjecture that the gap between  $e_g$  and  $t_{2g}$  subbands would not open up, irrespective of the strength of the  $p$  (anion) -  $d$  (cation) hybridization in the transition-metal compounds with the NaCl structure. This conjecture was based on the observation that, while the strong  $p$ - $d$  hybridization produces a large ligand-field splitting between  $e_g$  and  $t_{2g}$  subbands, the bandwidth of each subband becomes large at the same time. This conjecture was then one of the causes of Mattheiss's skepticism about the use of band theory for describing the electronic structure of insulating materials MnO, FeO, CoO, and NiO, particularly with reference to the insulating nature above the Néel temperature. An important contribution, which is favorable to band theory, was then made by Andersen *et al.*,<sup>17</sup> who showed that the lattice parameters of the insulating monoxides could be reproduced by the band-structure calculation. In particular, the sudden jump of the lattice parameter from VO to MnO was explained as a magnetic effect. However, their calculation for the ground-state antiferromagnetic orderings was not self-consistent either. (Recent self-consistent calculations by Yamashita and Asano<sup>18</sup> reproduced the observed lattice parameters very well; an almost identical result was obtained by our calculations also.)

In the first two of our series of papers,<sup>19,20</sup> we presented

some of the results of the self-consistent band-structure calculations for MnO,  $\alpha$ -MnS, and NiO in different magnetic states. We showed that the electronic structure is very sensitive to the magnetic ordering and that MnO and NiO can be insulators, but only when the magnetization is allowed to vary in the (111) direction, as it does in the experimentally observed ground state. We call this (111) variation AF II. We then estimated the interatomic magnetic coupling (the exchange interaction parameter in the Heisenberg Hamiltonian) for MnO,  $\alpha$ -MnS, and NiO with the use of the muffin-tin coherent-potential-approximation calculation. The theoretical results agree qualitatively with experimental results which were obtained from the spin-wave dispersion curves, thermodynamic analysis, etc.<sup>21</sup> Our band-theoretical treatment can give natural explanations of the rapid increase of the Néel temperature  $T_N$  from MnO ( $T_N=122$  K) to NiO ( $T_N=523$  K), and also to the small ferromagnetic first-nearest-neighbor coupling in NiO.

In the third paper of this series,<sup>22</sup> we demonstrated that a variety of experimental data can be consistently explained with a band picture. In particular, we pointed out that the experimental data of inverse photoemission<sup>11</sup> and two-phonon resonant-Raman scattering<sup>10</sup> indicate the presence of  $d^9$  states of Ni in NiO separated from the occupied  $d$  band only by  $\sim 2$  eV rather than by  $\sim 10$  eV (a typical value of the Coulomb integral  $U$  in the strong-correlation-limit picture). A small (effective)  $U$  of about 2 eV for transition-metal monoxides was supported also by Hüffner and Wertheim.<sup>23</sup> Therefore, we take the viewpoint that the effective intra-atomic Coulomb integral  $U$  and the energies pertaining to the cation  $d$  band are of comparable magnitude. This is in clear contrast to most of the existing Mott-insulator theories for these materials (see, for example, Brandow's review<sup>3</sup>).

The purpose of the present paper is to give a detailed description of the electronic structure obtained by band theory. In particular, we discuss in detail the reason why the antiferromagnetic ordering AF II is crucial to the insulating state of these oxides. A discussion will also be given on the possibility of having an insulating state for FeO and CoO from a band theory by taking account of the population imbalance in the minority-spin  $t_{2g}$  band induced by the intra-atomic exchange interaction. Our important conclusion here is that the difficulty in dealing properly with FeO and CoO lies in the local approximation in the spin-density-functional theory, and not in band theory itself. Analysis of experimental data based on the present band calculations was made in Ref. 22 and will be more extensively made in a subsequent paper.<sup>24</sup>

The band-structure calculations were done with the augmented-spherical-wave (ASW) method<sup>25</sup> and exchange and correlation were treated by the local-spin-density-functional (LSDF) formalism as described in Ref. 26. We use the lattice parameters listed in Table I of Ref. 15.

The organization of the present paper is as follows. We discuss the basic aspects of the band structure of MnO, FeO, CoO, and NiO in Sec. II by presenting several results of the band-structure calculation. In Sec. III we compare our results with some experimental results. We conclude in Sec. IV.

## II. RESULTS AND DISCUSSION OF BAND STRUCTURES

### A. MnO

#### 1. Overall aspects

Among the four materials (MnO, FeO, CoO, and NiO), MnO is the most easily tractable with regard to the insulating nature in a band picture and yet possesses very informative aspects. Therefore, we begin our discussion with MnO.

Figure 1 shows the total densities of states of MnO in four different magnetic orderings, the ferromagnetic state ( $F$ ), two antiferromagnetic states, the first kind (AF I) and the second kind (AF II), and the paramagnetic state. (The states below about 0.35 Ry are mostly O 2p and those above it are Mn 3d.) The antiferromagnetic ordering AF I and AF II are schematically shown in Fig. 2. Note that the actual orientation of the magnetic moment with regard to the crystal axis is irrelevant in the present work, because the spin-orbit interaction is not included in our band-structure calculations. A remarkable aspect of

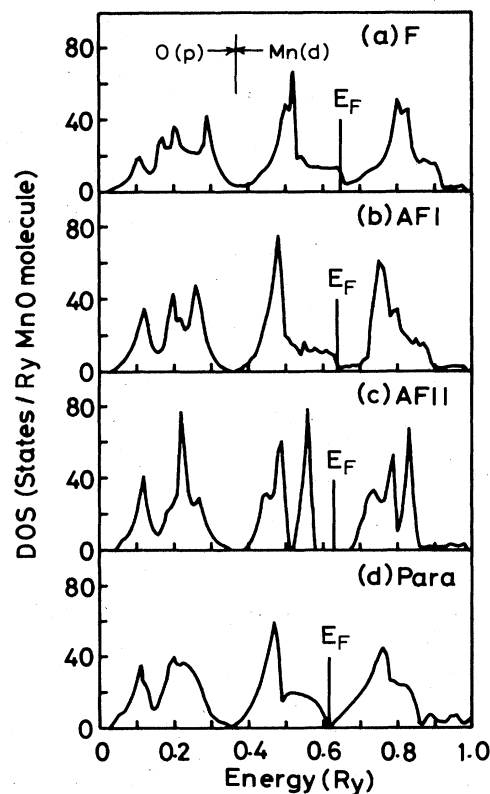


FIG. 1. (a) Total state densities of MnO (in states/Ry/MnO) in the ferromagnetic state, (b) in the antiferromagnetic states of the first kind, AF I, (c) of the second kind, AF II, and (d) in the paramagnetic state. The vertical lines denote the Fermi level.

Fig. 1 is that the ferromagnetic state  $F$  and the antiferromagnetic state AF I have similar densities of states and that there is no band gap at the Fermi energy, although the large exchange splitting makes them almost insulators. On the other hand, the antiferromagnetic state AF II, the observed ground-state configuration, has a very narrow  $e_g$  band and a well-defined band gap of  $\sim 0.1$  Ry. In the remainder of this section, we focus on the two problems: (i) Why is the  $e_g$  band in AF II so narrow compared with that in AF I or  $F$ ? (ii) Why is the AF II more stable than AF I or  $F$ ?

The schematic energy diagram in Fig. 3 summarizes the formation of  $d$  bands in the AF I and AF II structures from atomic levels by including interactions one at a time. We first take account of the exchange splitting  $\Delta_{\text{ex}}$  ( $=0.28$  Ry for MnO) and next the ligand-field splitting  $\Delta_{\text{lig}}$  ( $=0.08$  Ry for MnO) due to the octahedral cage of oxygen atoms surrounding a cation. Up to this point, there is no difference between AF I and AF II, because no intercation coupling has been taken into account. Important differences between AF I and AF II arise from the next step. First of all, we note that the strongest intercation hopping integral is of the  $dd\sigma$ -type between the second-nearest-neighbor cations which is mediated by the oxygen  $p$  orbital. The essential difference between AF I and AF II is that this strong  $dd\sigma$  interaction couples like polarized cation atoms in AF I, but couples exclusively oppositely magnetized cation atoms in AF II (see Fig. 2). Therefore,

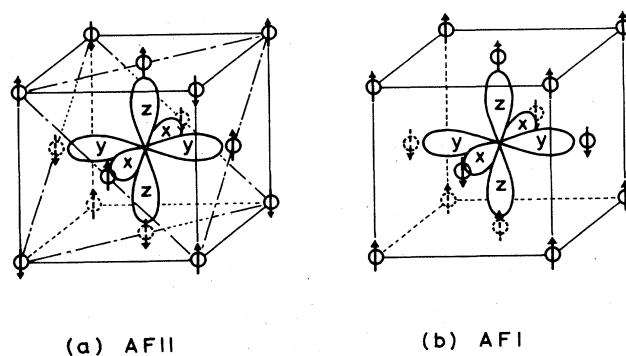


FIG. 2. Antiferromagnetic orderings of the second kind (AF II) and the first kind (AF I). AF II is the ground state ordering for MnO, FeO, CoO, and NiO. (Note that the spin and electronic quantization axes are independent, because of the neglect of the spin-orbit coupling in the present work.) As for the oxygen atoms, only the central one is shown for clarity. In the AF II (AF I) ordering, all three oxygen  $p$  orbitals couple action  $d$  states belonging to different (same) magnetic sublattices.

inclusion of the intersublattice coupling in AF II causes an appreciable energy shift of  $e_g$  states between the majority- and minority-spin bands, while it produces only a negligible effect in AF I. An important consequence of

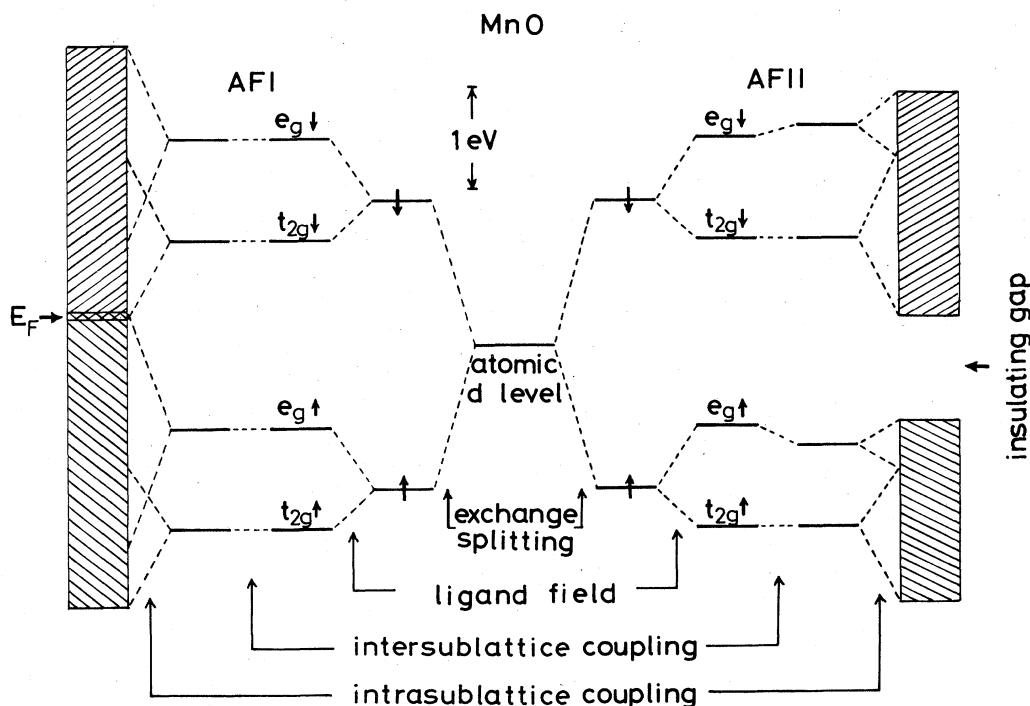


FIG. 3. Schematic diagram showing how the energy bands of  $d$  states in AF II and AF I are constructed by including interactions one at a time.

this intersublattice coupling is the stabilization of AF II compared with AF I and also  $F$ , due to a larger lowering of the occupied majority-spin  $e_g$  states. The final stage, where we take account of the intrasubband banding effect, the  $e_g$  subband becomes broader in AF I because of the strong  $dd\sigma$  coupling, while the absence of such intrasublattice  $dd\sigma$  coupling in AF II leads to a very narrow  $e_g$  subband. In addition to the exchange splitting  $\Delta_{ex}$ , the ligand-field splitting  $\Delta_{lig}$  is also an important factor for the narrow  $e_g$  band in the sense that  $\Delta_{lig}$  suppresses  $e_g$ - $t_{2g}$  hybridization. As for the width of the  $t_{2g}$  band, it comes

mostly from the direct first-nearest-neighbor cation-cation coupling and depends on the magnetic ordering only weakly.

The above qualitative arguments will be supplemented by the actual numerical calculations in the next two sections.

## 2. Intersublattice coupling

Figure 4(a) shows the partial density of states (PDOS) of  $d$  states,  $n_d(E)$ , in AF II of MnO. (See Appendix A for the precise definitions used in the state-density decom-

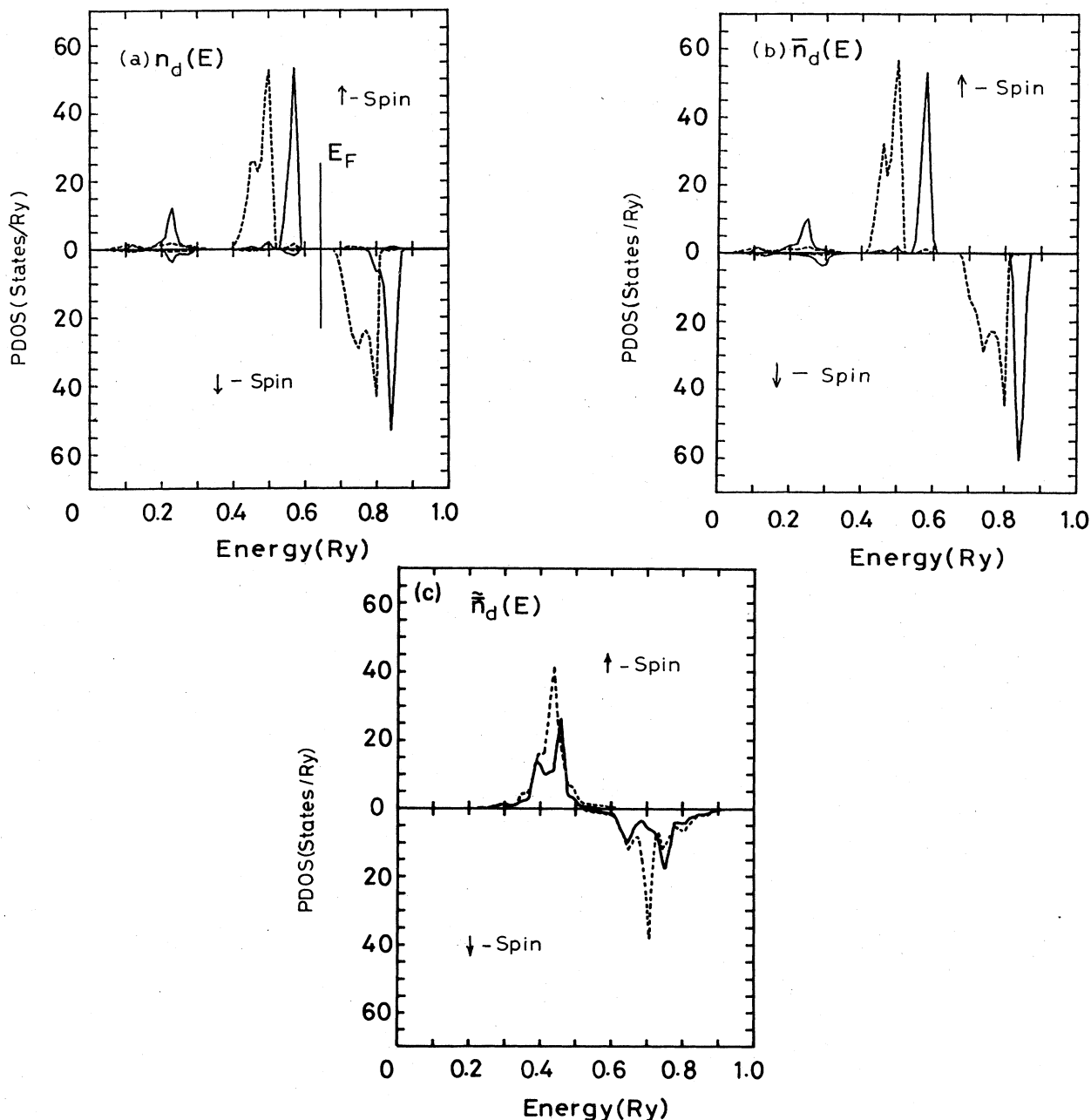


FIG. 4. Partial densities of states for Mn  $d$  orbitals in MnO: (a) in the actual AF II ordering,  $n_d(E)$ ; (b) in the absence of the intersublattice hybridization,  $\bar{n}_d(E)$ ; (c) for a spin-up magnetic moment sublattice decoupled from both spin-down magnetic moment sublattice and oxygen sublattice (approximately  $d$  PDOS of a single layer of spin-up magnetic moment Mn atoms). The solid (broken) lines denote  $e_g$  ( $t_{2g}$ ) contributions.

position.) The corresponding one without the intersublattice coupling,  $\bar{n}_d(E)$ , is shown in Fig. 4(b). Note that the strong second-nearest-neighbor  $dd\sigma$  coupling is completely absent in the case of Fig. 4(b) and the  $e_g$  band is very narrow. (The prescription for removing the intersublattice coupling is given in Appendix B.) At first glance,  $n_d$  is almost identical to  $\bar{n}_d$ , which implies that the effect of the intersublattice coupling is relatively weak. This is because the large exchange splitting  $\Delta_{ex}$  suppresses the intersublattice coupling  $dd\sigma$  (by a factor of  $dd\sigma/\Delta_{ex}=0.08$  in the second-order perturbation theory). The value for  $dd\sigma$  was taken from Ref. 15. The weak intersublattice coupling is consistent with the low Néel temperature of MnO ( $T_N=122$  K).<sup>19,20</sup> Nevertheless, by a careful inspection of Figs. 4(a) and 4(b), we notice that there are some differences between  $n_d$  and  $\bar{n}_d$  and that among these differences, the most significant consequence of the intersublattice coupling is the lowering of the majority-spin  $e_g$  band by about 0.02 Ry.

In order to compare the situation in AF II with that in AF I, we show  $n_d(E)$  and  $\bar{n}_d(E)$  for AF I in Figs. 5(a) and 5(b). As the strong  $dd\sigma$  coupling is already included in  $\bar{n}_d(E)$ , the  $e_g$  band is fairly wide and the difference between  $n_d$  and  $\bar{n}_d$  comes from other weaker couplings. Therefore, any difference in the  $e_g$  band between  $n_d$  and  $\bar{n}_d$  cannot be seen by eye, while small differences in the  $t_{2g}$  band exist. The argument in the preceding section about the stabilization of AF II compared with AF I (and *F*) was thereby substantiated.<sup>27</sup> Since the intersublattice hybridization is due to the spin-conserving electron hopping, it is an important concept that the magnetic ordering is determined by the spin-conserving interactions (as opposed to inter-atomic exchange interactions of the Coulomb-interaction origin).

### 3. Electronic structure of single metal layer

In the preceding section, we calculated the electronic structure of MnO, decoupling the intersublattice hybridization artificially. As a further analysis of the electronic structure, we decouple the oxygen-metal hybridization and calculate the electronic structure of an isolated single magnetic sublattice. (See Appendix B for further details.) From Fig. 2(a), we see that the interlayer distance within a given magnetic sublattice is very large, so that the interlayer interaction within a given sublattice may be negligibly small. Therefore, the PDOS of  $d$  states shown in Fig. 4(c) is approximately equal to the one for a single layer of (111) plane of Mn atoms. We note the following features in Fig. 4(c): (1) absence of ligand-field splitting of the  $d$  band; (2) a much wider  $e_g$  band compared with that of  $n_d$  in Figs. 4(a) and 4(b); (3)  $d$  density of states in Fig. 4(c) resembles a  $d$  resonance in a free-electron sea and the  $d$ -band tails from majority- and minority-spin bands overlap to fill the band gap; (4) the width of the  $d$  band in Fig. 4(c) is comparable to that of the  $t_{2g}$  band in Figs. 4(a) and 4(b); (5) the positions of the  $d$  bands are lower than those in Figs. 4(a) and 4(b). The first effect is natural, because there is no O(*p*)-Mn(*d*) hybridization. The second results from a large  $e_g$ - $t_{2g}$  hybridization caused by the first. The

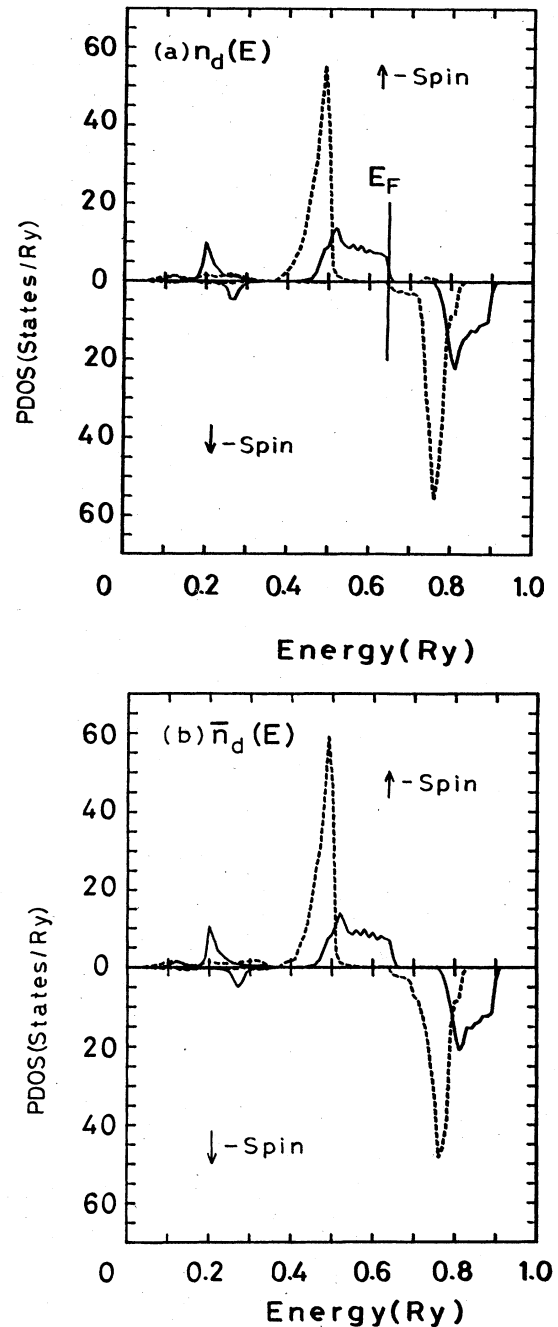


FIG. 5. Partial densities of states for Mn  $d$  orbitals: (a) in the actual AF I ordering,  $n_d(E)$ ; (b) in the absence of the intersublattice hybridization,  $\bar{n}_d(E)$ . The solid (broken) lines denote  $e_g$  ( $t_{2g}$ ) contributions.

third reflects the fact that, in the absence of oxygen, the bottom of the metal  $s$  band is lower than the  $d$  band, as in the pure transition metal. The fourth indicates that the bandwidth of the  $t_{2g}$  band in AF II (and also in AF I) comes mainly from the direct coupling of  $d$  orbitals belonging to the neighboring cations. The fifth is due to the absence of repulsion between Mn- $d$  states and O- $p$  states. The first three features are indicative of the important

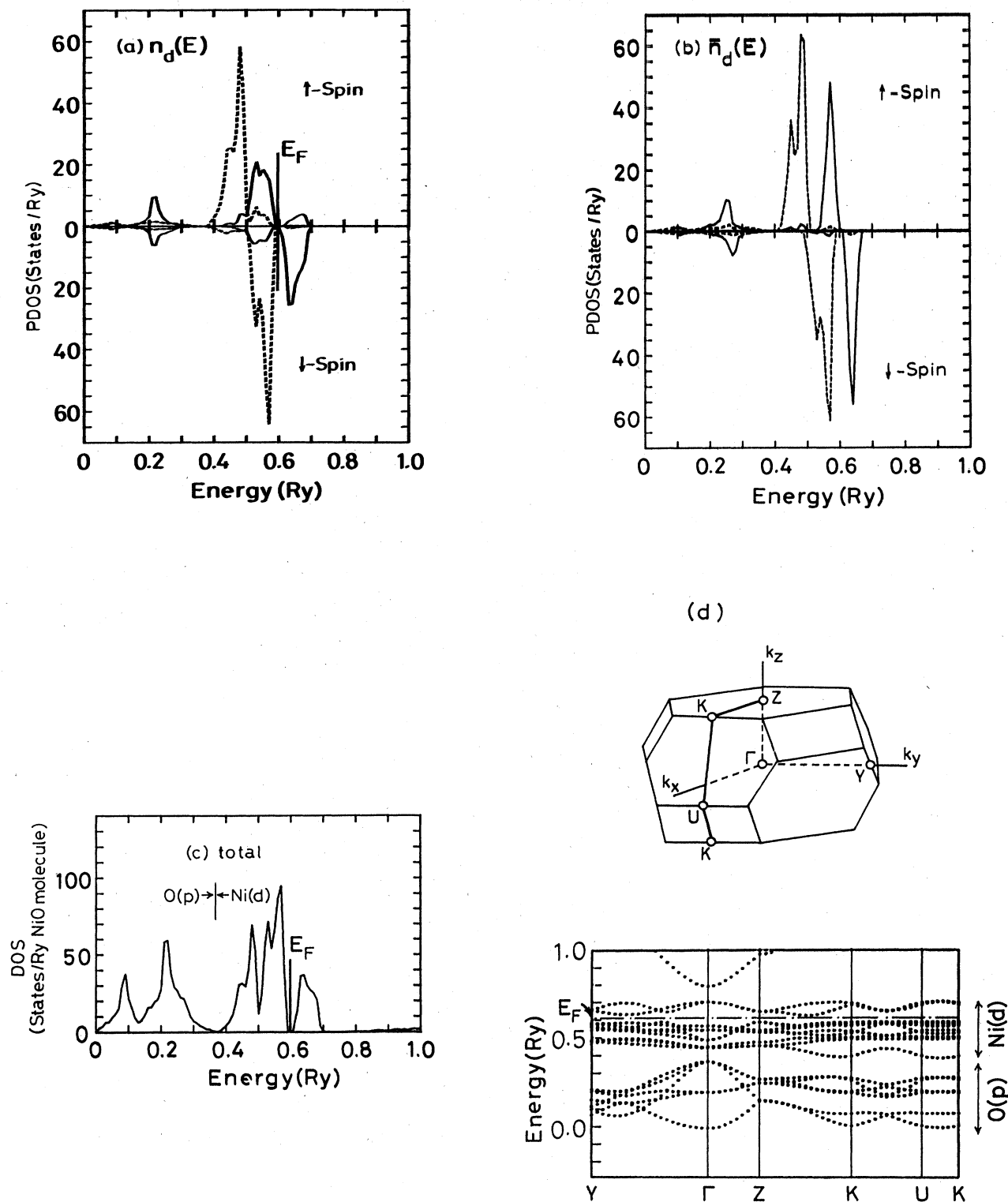


FIG. 6. (a) PDOS of Ni  $d$  orbitals in NiO in the actual AF II ordering,  $n_d(E)$ . (b) PDOS of Ni  $d$  orbitals in the absence of the intersublattice hybridization,  $\bar{n}_d(E)$ . In (a) and (b), the solid (broken) lines denote  $e_g(t_{2g})$  contributions. (c) Total density of states per NiO. (d) First Brillouin zone of rhombohedral crystal and the  $E$ - $\vec{k}$  curves for the AF II of NiO. The Fermi level  $E_F$  is shown by a chain line.

role of oxygen in realizing the insulator state of transition-metal monoxides.

### B. NiO

First, the narrow  $e_g$  band in AF II is crucial to the insulating nature of NiO, because the Fermi level lies in the  $e_g$ - $t_{2g}$  gap in the minority-spin band. It is also crucial to stabilizing the magnetic state. For example, the present band calculation does not produce the magnetic states of *F* and AF I.

Figures 6(a) and 6(b) show PDOS for NiO,  $n_d(E)$  and  $\bar{n}_d(E)$ , which correspond to those of MnO in Fig. 4. The total density of states per NiO and the  $E$ - $\vec{k}$  curves are also shown in Figs. 6(c) and 6(d). In contrast to the case of MnO, where the exchange splitting  $\Delta_{ex}$  dominates the ligand-field splitting  $\Delta_{lig}$  and width  $W_d$  of  $e_g$  and  $t_{2g}$  subbands,  $\Delta_{ex}$  in NiO is reduced, because of the smaller atomic magnetic moment, with the result that all of  $\Delta_{ex}$ ,  $\Delta_{lig}$ , and  $W_d$  are comparable in magnitude ( $\sim 1$  eV). A reduced  $\Delta_{ex}$  leads to a much larger intersublattice hybridization. Comparison of the ways of constructing energy bands from atomic levels between MnO and NiO (both in AF II) is schematically shown in Fig. 7. Several interesting aspects can be seen in Figs. 6 and 7. Already in  $\bar{n}_d$ , the majority-spin  $e_g$  band overlaps the minority-spin  $t_{2g}$  band, with the former at a slightly higher energy. The intersubband hybridization between  $e_g$  bands pushes the majority-spin  $e_g$  band to a lower energy to enhance the overlap between the majority-spin  $e_g$  and minority-spin  $t_{2g}$  bands, which consequently form a common band. It is

important to note that the fairly large  $e_g$  component of the minority spin in the energy range between 0.5–0.6 Ry is not due to the intrasubband  $e_g$ - $t_{2g}$  hybridization, but rather to the intersubband  $e_g$ - $e_g$  hybridization. The large energy lowering of the majority-spin  $e_g$  band by about 0.04 Ry stabilizes the antiferromagnetic ordering AF II and explains the strong antiferromagnetic coupling between the second-nearest-neighbor magnetic moments. In contrast to  $e_g$  band, the  $t_{2g}$  band is affected only slightly by the hybridization. Because the intersubband  $t_{2g}$ - $t_{2g}$  coupling is mainly due to the nearest-neighbor interaction, the small change in the  $t_{2g}$  band suggests a weak magnetic coupling between the nearest-neighbor atoms. Although the present analysis cannot predict the sign of the nearest-neighbor coupling, the above results are qualitatively consistent with the experimental results and our previous analysis.<sup>19,20,28</sup> The larger intersublattice  $e_g$ - $e_g$  hybridization due to a smaller exchange splitting in NiO compared with MnO explains also the difference in the Néel temperatures [ $T_N = 122$  K (MnO), 523 K (NiO)]. This aspect was discussed in our previous papers<sup>19,20</sup> in terms of the energy denominator in the perturbation treatment of the kinetic superexchange.

### C. FeO and CoO

Figures 8(a) and 9(a) show PDOS of  $d$  states for FeO and CoO in AF II. The Fermi energy lies inevitably within the minority-spin  $t_{2g}$  band which has a fairly high density of states and we end up with metallic FeO and CoO. The difficulty cannot be solved even if we take ac-

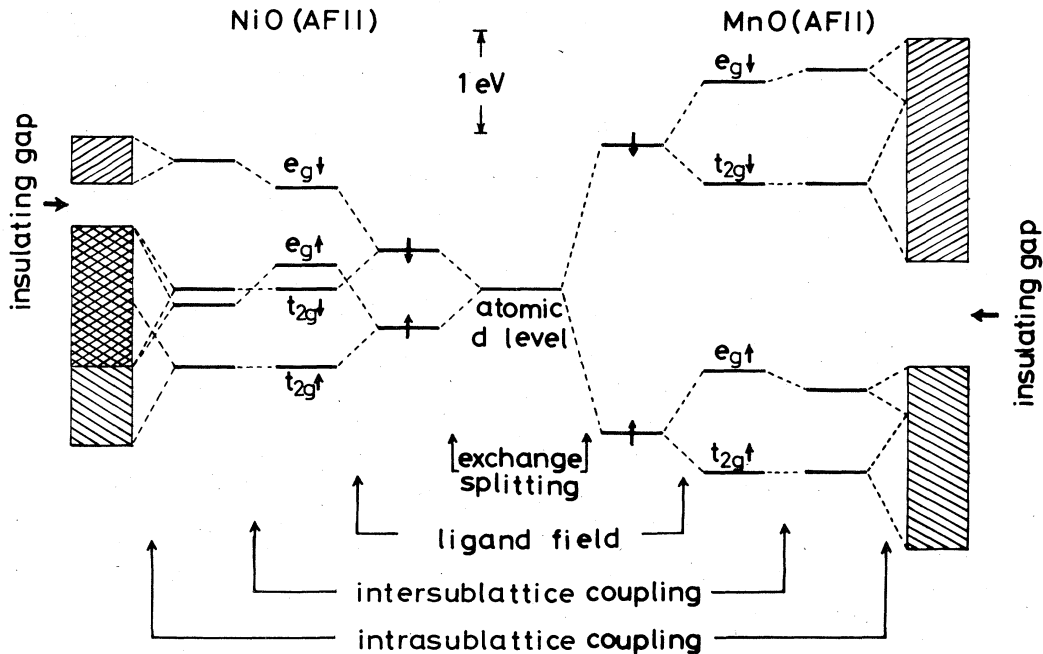


FIG. 7. Schematic diagram showing how the energy bands of  $d$  states are constructed in NiO and MnO with AF II structure. In the case of MnO, the exchange splitting dominates other energy scales, while in the case of NiO, the exchange splitting, ligand-field splitting and  $d$ -band width are all comparable in magnitude.



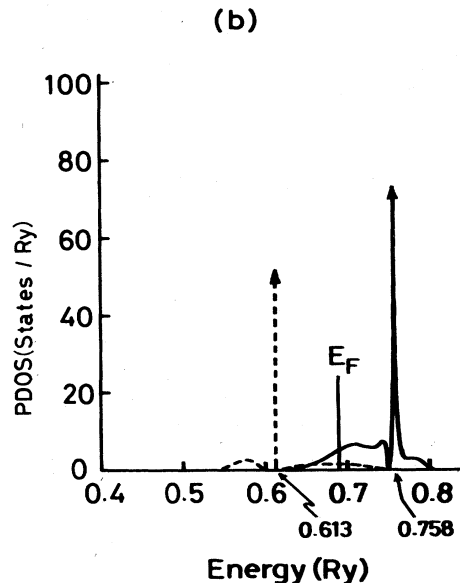
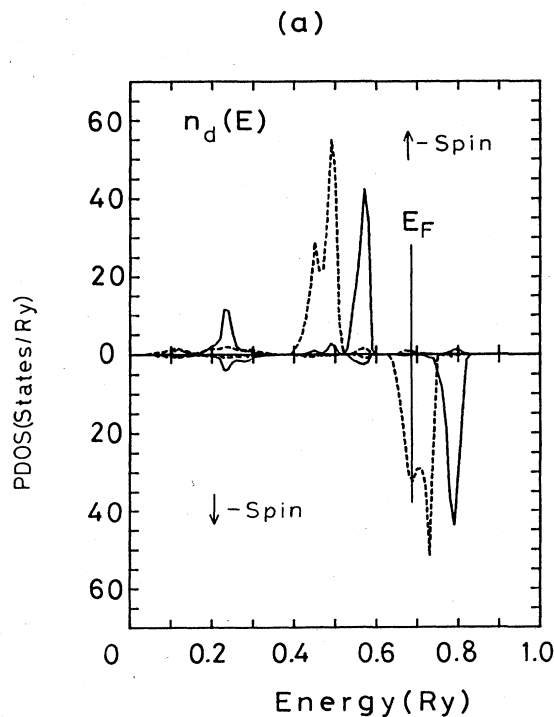


FIG. 8. PDOS of Fe  $d$  orbitals in FeO in the AF II ordering without population imbalance in the  $t_{2g}$  band of minority-spin state. The solid (broken) lines denote  $e_g$  ( $t_{2g}$ ) contributions. (b) PDOS of Fe  $t_{2g}$  orbitals of minority-spin state in FeO with population imbalance only at a given Fe site. The broken curve is a contribution from one of the  $t_{2g}$  orbitals which is almost filled and the solid curve is for the other two orbitals. The arrow at 0.613 Ry denotes a split-off state in a gap. There is also a very sharp structure at 0.758 Ry.

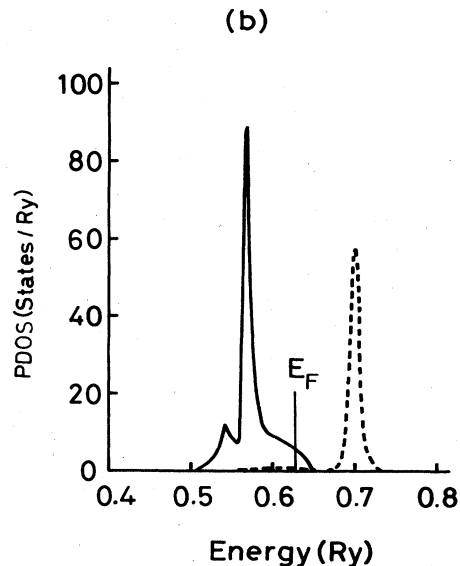
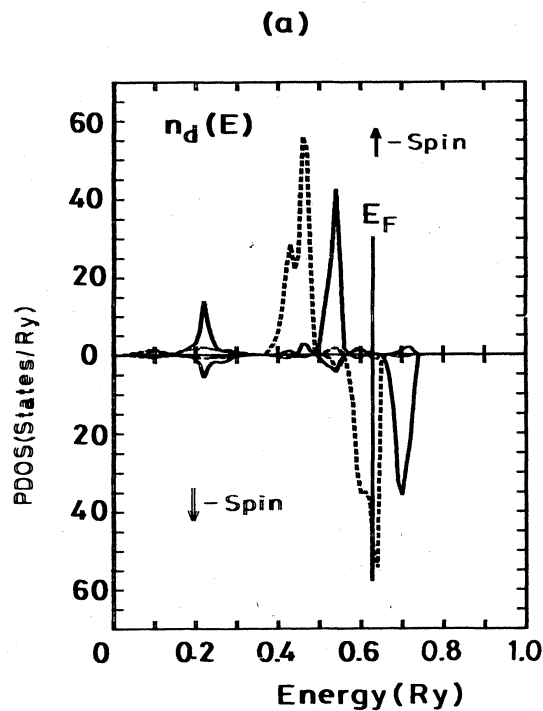


FIG. 9. (a) PDOS of Co  $d$  orbitals in CoO in the AF II ordering without population imbalance in the  $t_{2g}$  band of minority-spin state. The solid (broken) lines denote  $e_g$  ( $t_{2g}$ ) contributions. (b) PDOS of Co  $t_{2g}$  orbitals of minority-spin state in CoO with population imbalance only at a given Co site. The broken curve is a contribution from one of the  $t_{2g}$  orbitals which is almost empty and the solid curve is for the other two orbitals.

count of the lattice distortion from the cubic crystal. For instance, CoO has a tetragonal symmetry with  $c/a=0.988$  (Ref. 29). First of all, the distortion seems to be too small to produce a gap in  $t_{2g}$  band. Besides, even if the ligand field is strong enough to produce a gap, we expect that  $yz$  and  $zx$  orbitals in the  $t_{2g}$  states will have a higher energy than the  $xy$  orbital for the distortion of  $c/a < 1$ . As the  $t_{2g}$  band has to accommodate two electrons per metal atom, the Fermi energy must be at the middle of the degenerate  $yz$  and  $zx$  bands. With these considerations, it has been generally thought that the band theory would never explain the insulating nature of FeO and CoO and that the partial success of the band theory for MnO and NiO would be only accidental.<sup>3</sup>

We take an opposite viewpoint. We admit that the band theory is not the whole story and that correlation effects beyond the local-density-functional theory will reduce the band width to some extent. However, we found in the previous sections, the insulating nature and the magnetic ordering of MnO and NiO can be explained in a quite natural way within the band picture. This encourages us to think that the band theory should at least indicate an inclination of FeO and CoO to becoming an insulator. The key which has been missing is the presence of a fairly large unquenched orbital angular momentum in both materials. An extensive study of the orbital angular momentum in CoO was made by Kanamori.<sup>30</sup> The fundamental implication of a significant orbital moment in the present context is the instability to the population imbalance in the minority-spin  $t_{2g}$  band induced by the intra-atomic exchange interaction. By using the Anderson model or the tight-binding model with degenerate orbitals, it was shown that the condition of the population imbalance is given by<sup>31-33</sup>

$$n(E_F)(U-J) > 1, \quad (1)$$

where  $n(E_F)$  is the density of states per spin and per orbital at the Fermi level.  $U$  and  $J$  are the Coulomb and exchange integrals. Yosida *et al.*<sup>32</sup> analyzed the anisotropy energy of transition-metal impurities in Co metal and estimated the values of  $U-J$  as 2 eV, with  $U$  and  $J$  as 3 and 1 eV, respectively, for the  $3d$  transition elements. With the use of  $n(E_F)$  obtained by the present band calculations, we obtain

$$n(E_F)(U-J) = \begin{cases} 2.5, & \text{for CoO,} \\ 1.8, & \text{for FeO.} \end{cases} \quad (2)$$

Therefore, we expect that FeO and CoO are unstable with regard to the population imbalance in the  $t_{2g}$  band, which indicates the possibility of opening up a gap at the Fermi level.

One of the ways of checking the reliability of the above values of  $U$  and  $J$  is to study the Stoner criterion for the instability to the formation of the spin-magnetic moment, for which analyses based on the local-spin-density-functional formalism are also available.<sup>34,35</sup> The condition is given by

$$n(E_F)(U+4J) > 1, \quad (4)$$

where the factor of 4 before  $J$  is obtained for the  $d$ -band case. First we note that the exchange integral  $I$  by Janak<sup>34</sup> corresponds to  $(U+4J)/10$ , because Janak used the density of states which includes both the spin and the orbital degeneracies. The estimate by Yosida *et al.* of  $U$  and  $J$  gives  $(U+4J)/10=0.052$  Ry, which is about 1.4 times larger than Janak's  $I$  of 0.036 Ry. The use of the above values for  $U$  and  $J$  is, however, rather reasonable for FeO and CoO, because it is generally expected that  $U$  and  $J$  will take larger values in compounds (than in pure metals), due to the absence of the screening effects of  $s$  electrons. We note also that even if we reduce  $U-J$  by 1.4, the condition of Eq. (1) is still satisfied for FeO and CoO.<sup>36</sup>

Deferring a more extensive study to future work, we present here some results obtained by a simple model calculation in order to demonstrate the significance of the population imbalance for making FeO and CoO insulators. What we do is as follows. We take account of the possibility of the population imbalance only at a given Co (or Fe) site, leaving other sites as shown in Figs. 8(a) and 9(a). Therefore the problem is reduced to an impurity problem and we solve it approximately by using linear combination of atomic orbitals (LCAO) formalism, which will work for the narrow  $t_{2g}$  band of present interest. The inputs to the calculation are the PDOS of  $t_{2g}$  [Figs. 8(a) or 9(a)] and the value of  $U-J$ . By setting  $U-J=2$  eV, a self-consistent solution with the population imbalance in the minority-spin  $t_{2g}$  band is shown in Figs. 8(b) and 9(b) for FeO and CoO, respectively. Because this is an impurity problem, the density of states at the central site (impurity site) cannot have a gap at the Fermi level. Nevertheless, it is clear that the PDOS of  $t_{2g}$  in Figs. 8(b) and 9(b) consists of two almost separate bands with very small values of state densities at the Fermi level. If the population imbalance occurs at every site, each of the sharp separate states will become broader but the tails will shrink and thereby a gap will open up at the Fermi level.

One may think that we should do the above analysis within the framework of the local-spin-density-functional formalism. Unfortunately, the LSDF formalism is not adequate for the estimation of the energy change caused by the symmetry breaking in the charge distribution.<sup>37</sup> Actually our estimation by the LSDF of the quantity corresponding to  $U-J$  turned out to be negative, which is apparently unphysical (see Appendix C). We have to go beyond the LSDF formalism in order to deal with the unquenched orbital angular momentum properly. We are claiming that the present difficulty in dealing with FeO and CoO lies in the local approximation of the density-functional theory, but not in the band theory itself.

### III. COMPARISON WITH SOME EXPERIMENTAL DATA

Since extensive analyses of experimental data are made in other papers,<sup>22,24</sup> here we only present calculated results for the magnitude of the local magnetic moment of cation and also for the ligand-field splitting.

### A. Magnitude of the cation magnetic moment

Experimentally, the magnitude of the magnetic moment associated with a cation is obtained by the analysis of the magnetic form factor. The experimental values (in  $\mu_B$ ) are 4.79 for MnO (Ref. 38), 1.64 (Ref. 39) and 1.77 (Ref. 38) for NiO, and 3.35 (Ref. 40) for CoO. [In the case of NiO, the spin-magnetic moment was obtained by taking account of the  $g$  factor of 2.2 (Ref. 39) and the value for CoO includes a contribution from the orbital angular momentum.] The experimental value for FeO is not available to our knowledge.

In our band-structure calculation, the magnetic moment of a metal atom,  $M_{loc}$ , is defined as the spin magnetic moment within the atomic sphere of metal atom. Naively, one may think that  $M_{loc}$  would simply be 5 and 2 for MnO and NiO, respectively, because a gap exists at the Fermi level. This is not true. First, the intersubband hybridization introduces a mixing between the local majority- and minority-spin states. Therefore, in the occupied Mn  $d$  bands, there is a small contribution from the local minority-spin states, which reduces the value of  $M_{loc}$ . In addition, there is also a contribution from the hybridization with the oxygen  $p$  states, which do not have spin polarization. In this way,  $M_{loc}$  for Mn is reduced to 4.45. Similarly,  $M_{loc}$  for other materials are 3.43 (FeO), 2.35 (CoO), and 1.09 (NiO). We see that the experimental values listed above are larger than the theoretical  $M_{loc}$ , particularly for NiO. (We leave the discussion of FeO and CoO to a future work.) It is important to note here that  $M_{loc}$  depends on the choice of atomic radius of each species, and does not exactly correspond to the experimental values. Figure 10 shows the dependence of  $M_{loc}$  on the ratio of atomic radii  $R_{Ni}/R_O$  for NiO with a fixed lattice constant. The amount of charge transfer  $Q$  from an atomic sphere of Ni to that of O is also shown. Our usual prescription for determining atomic radius for each element in a compound<sup>41</sup> gives 1.13 as  $R_{Ni}/R_O$  and Pauling's ionic radii for  $Ni^{2+}$  and  $O^{2-}$  give about 0.5.<sup>42</sup> The rather sensitive dependence of  $M_{loc}$  on the choice of atomic radii comes from the spatial spin polarization around oxygen atoms, although they do not have net spin polarization. When we change the radius of the atomic sphere of oxygen, the spatial spin polarization around oxygen makes a contribution to  $M_{loc}$  of metal atom effectively. This implies deviations from the spherical-potential approximation used in the present band calculation. It is one of our future projects to calculate the spin-density distribution or the magnetic form factor with the

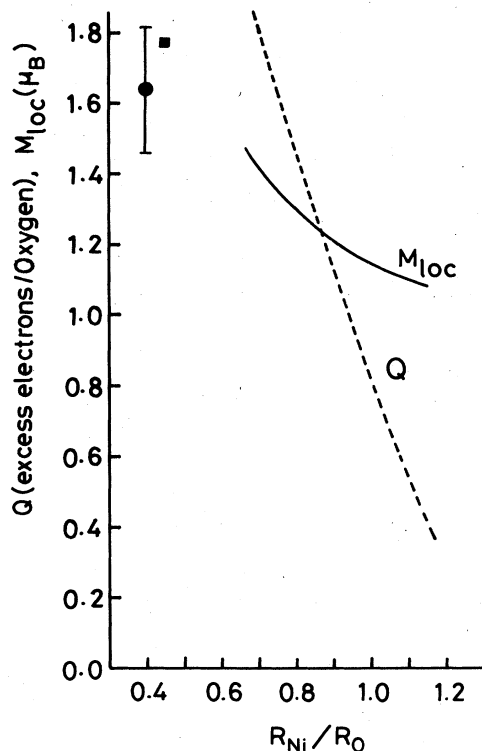


FIG. 10. Spin magnetic moment within the atomic sphere of Ni in NiO,  $M_{loc}$  (in  $\mu_B$ ), and the electron transfer from Ni to O,  $Q$ , are shown as functions of  $R_{Ni}/R_O$ . The experimental data for Ni magnetic moment are shown also by a square (Ref. 38) and a circle with an error bar (Ref. 39).

use of a more general form of the potentials in the band calculation and thereby to make a direct comparison with theory and experiment.

### B. Ligand-field splitting

Table I shows the ligand-field-splitting data. Theoretical values were obtained by calculating the difference in the energy of the centers of gravity of  $t_{2g}$  and  $e_g$  bands. The agreement between theory and experiment is satisfactory. It should be noted that the  $t_{2g}$ - $e_g$  splitting is entirely due to the  $p$ - $d$  covalency effect in the present calculation, because of the use of the spherical potential for metal atoms. Because the charge associated with oxygen spreads widely in space, the electrostatic contribution to the ligand-field splitting must be very small. In contrast to our results, Mattheiss<sup>16</sup> underestimated the ligand-field splitting. The main source of this discrepancy is his underestimation of the  $p$ - $d$  covalency effect due to a much larger energy separation between oxygen  $p$  band and metal  $d$  band in his band scheme.

## IV. CONCLUSIONS

We have shown that the band theory based on the LSDF formalism accounts well for the insulating nature of MnO and NiO in their ground-state magnetic ordering

TABLE I. Theoretical and experimental ligand-field splitting in the ground state (in Ry).

	MnO	FeO	CoO	NiO
Theory	0.077	0.084	0.085	0.099
Experiments <sup>a</sup>	0.089		0.086	0.083
	0.092			0.081
				0.080

<sup>a</sup>Experimental data are borrowed from Table I in Ref. 16.

AF II. The antiferromagnetic ordering AF II is special in the sense that it makes the  $e_g$  band particularly narrow. This is a crucial condition for making MnO and NiO insulators. The reasons for the narrow  $e_g$  band in AF II and the stability of AF II were analyzed in detail. As for the insulating nature of FeO and CoO, we pointed out the possibility of having a population imbalance among the  $t_{2g}$  states, which is induced by the intra-atomic exchange interaction and is related to the unquenched orbital angular momentum in these materials. We showed that the partial density of states from the present band calculation satisfies the criterion for the instability for the population imbalance for the values of the Coulomb and exchange integrals,  $U$  and  $J$ , estimated from the anisotropy energy of transition-metal impurities in metallic cobalt.<sup>32</sup> (Note that we assumed that  $U - J$  is 2 eV rather than about 10 eV, the latter being the commonly used value in strong correlation-limit picture.<sup>3,36</sup>) We then demonstrated by a model calculation that the population imbalance splits the minority-spin  $t_{2g}$  band into two almost separate subbands with only a very small density of states at the Fermi level. However, the LSDF formalism leads us to a rather unphysical result in this problem (Appendix C).<sup>37</sup>

We showed that the ligand-field splitting calculated by our band calculations agrees fairly well with observed one. An important concept here is that the covalency effect between oxygen  $p$  states and metal  $d$  states is the dominant source of the ligand-field splitting. Calculated local magnetic moment is generally smaller than that observed by neutron diffraction. However, it was pointed out that some fundamental difficulties exist in making a direct comparison of the cation magnetic moment between theory and experiment.

In a subsequent paper, we will give an extensive analysis of experimental data from our band scheme, discuss some possible mechanisms to sustain the insulating nature even above the Néel temperature and show that the oxides MnO, FeO, CoO, and NiO are much less special than is generally thought.

*Note added in proof.* After submission of the manuscript, S. Wakoh informed us of his work about the population imbalance in CoO [S. Wakoh, J. Phys. F 7, L15 (1977)].

#### ACKNOWLEDGMENTS

The authors would like to thank N. Hamada for valuable comments and discussions. They are also grateful to V. Moruzzi for invaluable help with the numerical computations. This work was initiated while one of the authors (K.T.) was visiting at the IBM Thomas J. Watson Research Center (Yorktown Heights). He would like to express his sincere thanks to the IBM World Trade Corporation for supporting his stay here. This work was supported in part by a Grant-in-Aid for Cooperative Research from the Ministry of Education, Science and Culture of Japan.

#### APPENDIX A: PARTIAL-DENSITY-OF-STATES (PDOS) DECOMPOSITION IN AF II

In the PDOS shown in Figs. 4, 5, 6, 8, and 9,  $e_g$  and  $t_{2g}$  states are referred to with regard to the cubic axes of the

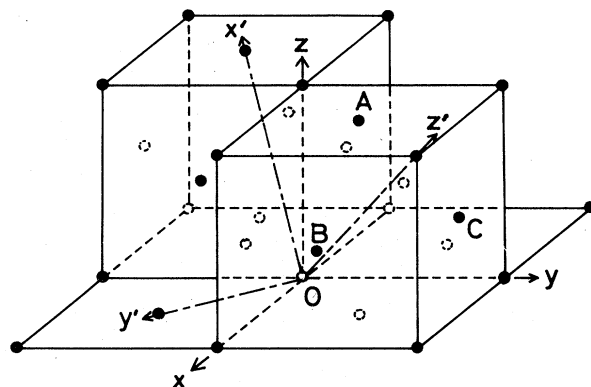


FIG. 11. Relation of two coordinate systems. The  $x$ ,  $y$ , and  $z$  axes are along the cubic crystal axes. The  $x'$ ,  $y'$ , and  $z'$  axes are taken so that the  $z'$  axis is the threefold rotation axis, the  $z'$ - $x'$  plane is the mirror plane, and the  $y'$  axis is the twofold rotation axis in the case of the AF II ordering. Only the cations are shown by circles.

NaCl structure. As the point-group symmetry of the AF II is  $D_{3d}$ , the orbitals belonging to  $e_g$  and  $t_{2g}$  are not the basis functions of the irreducible representations of  $D_{3d}$ . By taking the new  $x'$ ,  $y'$ , and  $z'$  axes, as shown in Fig. 11 [( $z'$ ,  $x'$ ) plane is the mirror plane and  $y'$  axis is the twofold rotation axis], the five  $d$  orbitals are categorized into three groups according to the irreducible representations of  $D_{3d}$ :  $|3(z')^2 - r^2\rangle$ ,  $A_1$ ;  $|y'z'\rangle$  and  $|z'x'\rangle$ ,  $E(1)$ ;  $|x'y'\rangle$  and  $-(x')^2 - (y')^2$ ,  $E(2)$ .

The argument of  $E$  identifies two different sets of basis functions belonging to the irreducible representation  $E$ . The above  $d$  orbitals are expressed by  $e_g$  and  $t_{2g}$  orbitals as

$$\begin{aligned} |3(z')^2 - r^2\rangle &= (|xy\rangle + |yz\rangle + |zx\rangle)/\sqrt{3}, \\ |y'z'\rangle &= (2|x^2 - y^2\rangle - |yz\rangle + |zx\rangle)/\sqrt{6}, \\ |z'x'\rangle &= \sqrt{2/3} |3z^2 - r^2\rangle \\ &\quad - (\sqrt{2}/6)(2|xy\rangle - |yz\rangle - |zx\rangle), \\ |x'y'\rangle &= -( |x^2 - y^2\rangle + |yz\rangle - |zx\rangle )/\sqrt{3}, \\ |(x')^2 - (y')^2\rangle &= (1/\sqrt{3}) |3z^2 - r^2\rangle \\ &\quad + (1/3)(2|xy\rangle - |yz\rangle - |zx\rangle). \end{aligned}$$

We take linear combinations between  $E(1)$  and  $E(2)$  to obtain the following new set of functions:

$$\begin{aligned} \phi_1 &= (1/\sqrt{3})(|xy\rangle + |yz\rangle + |zx\rangle) \\ &= |3(z')^2 - r^2\rangle, \\ \phi_2 &= (1/\sqrt{2})(|zx\rangle - |yz\rangle) \\ &= (1/\sqrt{3})(|y'z'\rangle + \sqrt{2}|x'y'\rangle), \\ \phi_3 &= (1/\sqrt{6})(-2|xy\rangle + |yz\rangle + |zx\rangle) \\ &= (1/\sqrt{3})[|z'x'\rangle - \sqrt{2}|(x')^2 - (y')^2\rangle], \end{aligned}$$

$$\begin{aligned}\phi_4 &= |x^2 - y^2\rangle = (1/\sqrt{3})(\sqrt{2}|y'z'\rangle - |x'y'\rangle), \\ \phi_5 &= |3z^2 - r^2\rangle \\ &= (1/\sqrt{3})[\sqrt{2}|z'x'\rangle + |(x')^2 - (y')^2\rangle].\end{aligned}$$

The PDOS of  $t_{2g}$  and  $e_g$  are defined as

$$\begin{aligned}n_{t_{2g}} &= -(1/\pi)\text{Im}(\langle xy | G | xy \rangle + \langle yz | G | yz \rangle \\ &\quad + \langle zx | G | zx \rangle), \\ n_{e_g} &= -(1/\pi)\text{Im}(\langle x^2 - y^2 | G | x^2 - y^2 \rangle \\ &\quad + \langle 3z^2 - r^2 | G | 3z^2 - r^2 \rangle),\end{aligned}$$

where  $G$  is the Green function of the system. It is now straightforward to show that

$$\begin{aligned}n_{t_{2g}} &= -(1/\pi)\text{Im}(\langle \phi_1 | G | \phi_1 \rangle \\ &\quad + \langle \phi_2 | G | \phi_2 \rangle + \langle \phi_3 | G | \phi_3 \rangle) \\ &= n_{A_1} + \frac{1}{3}(n_{E(1)} + 2n_{E(2)} + 2\sqrt{2}n_{E(1-2)}), \\ n_{e_g} &= -(1/\pi)\text{Im}(\langle \phi_4 | G | \phi_4 \rangle + \langle \phi_5 | G | \phi_5 \rangle) \\ &= \frac{1}{3}(2n_{E(1)} + n_{E(2)} - 2\sqrt{2}n_{E(1-2)}),\end{aligned}$$

where

$$\begin{aligned}n_{A_1} &= (1/\pi)\text{Im}\langle 3(z')^2 - r^2 | G | 3(z')^2 - r^2 \rangle, \\ n_{E(1)} &= -(1/\pi)\text{Im}(\langle y'z' | G | y'z' \rangle \\ &\quad + \langle z'x' | G | z'x' \rangle), \\ n_{E(2)} &= -(1/\pi)\text{Im}[\langle x'y' | G | x'y' \rangle \\ &\quad + \langle (x')^2 - (y')^2 | G | (x')^2 - (y')^2 \rangle], \\ n_{E(1-2)} &= -(1/\pi)\text{Im}[\langle y'z' | G | x'y' \rangle \\ &\quad - \langle z'x' | G | (x')^2 - (y')^2 \rangle].\end{aligned}$$

$n_{A_1}$ ,  $n_{E(1)}$ ,  $n_{E(2)}$ , and  $n_{E(1-2)}$  can be obtained by the  $k$ -space integration in the irreducible part of the Brillouin zone. The off-diagonal part  $n_{E(1-2)}$  makes a significant contribution.

In the actual density-of-states (DOS) or PDOS calculations for the AF II structure, 810  $\vec{k}$  points, which are equally spaced in the irreducible part of the Brillouin zone, are used and the spectral weight corresponding to each eigenstate is broadened by an isosceles triangle with the base width of 0.01 Ry. (Therefore, in the DOS curves, a gap is smaller than the real value. However, the value of a gap referred to in the text is obtained by sampling the highest occupied eigenenergy and the lowest unoccupied one and is not affected by the broadening effect.) For the AF I structure, 550  $\vec{k}$  points are used.

#### APPENDIX B: COMMENTS ON $n_d(E)$ AND $\bar{n}_d(E)$ IN FIGS. 4–6

The secular equation in augmented spherical waves<sup>25</sup> (ASW) can be formally written as

$$\det \begin{bmatrix} A_{M1,M1} & A_{M1,M2} & A_{M1,O} \\ A_{M2,M1} & A_{M2,M2} & A_{M2,O} \\ A_{O,M1} & A_{O,M2} & A_{O,O} \end{bmatrix} = 0, \quad (B1)$$

where the subscript  $M1$  ( $M2$ ) denotes the metal sublattice of  $\uparrow$  ( $\downarrow$ ) magnetic moment in Fig. 2 and the subscript  $O$  the oxygen sublattice. By using the matrix transformation of Eq. (27) of Ref. 43, we can fold the oxygen subspace into the metal subspace and reduce (B1) into

$$\det \begin{bmatrix} B_{M1,M1} & B_{M1,M2} \\ B_{M2,M1} & B_{M2,M2} \end{bmatrix} = 0, \quad (B2)$$

with

$$B_{Mi,Mj} = A_{Mi,Mj} - A_{Mi,O}(A_{O,O})^{-1}A_{O,Mj}. \quad (B3)$$

The off-diagonal blocks  $B_{M1,M2}$  and  $B_{M2,M1}$  contribute to the intersublattice hybridization.  $n_d(E)$  in Figs. 4–6, are obtained from either (B1) or (B2) and its counterpart  $\bar{n}_d(E)$  from either

$$\det(B_{M1,M1}) = 0, \quad (B4)$$

or

$$\det \begin{bmatrix} A_{M1,M1} & A_{M1,O} \\ A_{O,M1} & A_{O,O} \end{bmatrix} = 0. \quad (B5)$$

Furthermore, the  $d$  PDOS of Fig. 4(c) is calculated simply by

$$\det(A_{M1,M1}) = 0. \quad (B6)$$

An additional comment on (B5) and (B6) is that the matrix elements in (B5) and (B6) are not exactly the same as the corresponding ones in (B1). In the ASW formalism,<sup>25</sup> the  $M2$  sublattice makes some contribution to, for example,  $A_{M1,M1}$ . [This comes from the sum over  $\nu''$  in Eq. (29) of Ref. 25.] Such a contribution is included in (B1), but is artificially neglected in (B5). In (B6), contributions from both of  $M2$  and oxygen sublattices to  $A_{M1,M1}$  are neglected.

#### APPENDIX C: A NOTE ON THE LSDF APPROACH TO THE ARGUMENT IN SEC. II C

Let us assume the charge-density fluctuation at a Co site represented by

$$\begin{aligned}\delta\rho(\vec{r}) &= \delta n \{ -[Y_{yz}(\vec{r})]^2 + 0.5[Y_{xy}(\vec{r})]^2 \\ &\quad + 0.5[Y_{zx}(\vec{r})]^2 \} [R_d(r;E_F)]^2, \quad (C1)\end{aligned}$$

where  $Y_L(\vec{r})$  denotes the real spherical harmonics and  $R_d(r;E_F)$  is the radial wave function of Co with the Fermi energy which is normalized to unity within the atomic sphere.  $\delta\rho(\vec{r})$  of (C1) represents the situation where a fractional charge  $\delta n$  is transferred from the  $yz$  state to the  $xy$  and  $zx$  states. If CoO is unstable with respect to this charge fluctuation, a situation where the  $yz$  state will have a higher energy than the  $xy$  and  $zx$  states will be spontaneously realized and there is a possibility of having a gap which separates the unoccupied  $yz$  state from the occupied  $xy$  and  $zx$  states.  $\delta\rho$  of (C1) will give the energy shift  $\delta\epsilon$  for the  $yz$  orbital given as

$$\delta\epsilon = \left\langle yz \left| \left[ \frac{\partial U_{xc}}{\partial \rho} \delta\rho(\vec{r}) + 2 \int \frac{\delta\rho(\vec{r}')}{|\vec{r} - \vec{r}'|} d^3r' \right] \right| yz \right\rangle. \quad (C2)$$

The criterion for the charge imbalance is given by

$$n_{yz}(E_F)\delta\epsilon > \delta n, \quad (C3)$$

where  $n_{yz}$  is the PDOS for the  $yz$  orbital. We can reduce (C3) to

$$n_{yz}(E_F) \{ \delta\epsilon(\text{Coul})_{\text{off-dia}} - [\delta\epsilon(\text{Coul})]_{\text{dia}} \} + \{ [\delta\epsilon(\text{XC})]_{\text{off-dia}} - [\delta\epsilon(\text{XC})]_{\text{dia}} \} > 1, \quad (C4)$$

which corresponds to Eq. (1). In (C4), the subscript dia denotes the contribution to  $\delta\epsilon$  of (C2) from the charge fluctuation associated with the  $yz$  orbital and the subscript off-dia denotes the contribution from the  $xy$  or  $zx$  orbital. The quantities in (C4) are expressed as

$$[\delta\epsilon(\text{Coul})]_i = \sum_{l=0,2,4} \alpha_{l,i} \lambda_l, \quad i = \text{off-dia or dia},$$

with

$$\lambda_l = 2 \int_0^R dr [R_d(r; E_F)]^2 \times \left[ r^{1-l} \int_0^r [R_d(r'; E_F)]^2 (r')^{l+2} dr' + r^{l+2} \int_r^R [R_d(r'; E_F)]^2 (r')^{1-l} dr' \right],$$

$$\alpha_{l,\text{dia}} = \begin{cases} 1, & l=0, \\ \frac{4}{49}, & l=2,4, \end{cases}$$

$$\alpha_{l,\text{off-dia}} = \begin{cases} 1, & l=0, \\ -\frac{2}{49}, & l=2, \\ -\frac{4}{441}, & l=4, \end{cases}$$

and

$$[\delta\epsilon(\text{XC})]_{\text{dia}} = \left( \frac{15}{28} \pi \right) \eta,$$

$$[\delta\epsilon(\text{XC})]_{\text{off-dia}} = \left( \frac{5}{28} \pi \right) \eta,$$

with

$$\eta = \int_0^R \frac{\partial U_{xc}}{\partial \rho} [R_d(r; E_F)]^4 r^2 dr.$$

With the use of the self-consistent potential for Co, we estimated  $\lambda_l$  and  $\eta$  as (in Ry)

$$\lambda_l = \begin{cases} 1.8360, & l=0 \\ 0.8385, & l=2 \\ 0.5195, & l=4 \end{cases}$$

and

$$\eta = -1.0184.$$

With these values we obtain

$$[\delta\epsilon(\text{Coul})]_{\text{dia}} = 1.9468,$$

$$[\delta\epsilon(\text{Coul})]_{\text{off-dia}} = 1.7970,$$

$$[\delta\epsilon(\text{XC})]_{\text{dia}} = -0.1737,$$

$$[\delta\epsilon(\text{XC})]_{\text{off-dia}} = -0.0579,$$

in Ry and the value in the bold parentheses on the left-hand-side of (C4) is  $-0.034$  Ry. This value corresponds to  $U - J$  in Eq. (1) and the negative value is unphysical. One of the shortcomings of the present scheme compared with that in Sec. II C, which is based on the Hartree-Fock scheme, is due to the nonvanishing contribution of the self-energy.

\*Present address: Department of Physics and Astronomy, Northwestern University, Evanston, IL 60201.

<sup>1</sup>N. F. Mott, Proc. Phys. Soc. London Ser. A **62**, 416 (1949).

<sup>2</sup>D. Adler, *Solid State Physics*, edited by F. Seitz and D. Turnbull (Academic, New York, 1968), Vol. 21, p. 1.

<sup>3</sup>B. H. Brandow, Adv. Phys. **26**, 651 (1977).

<sup>4</sup>A. B. Kunz and G. T. Surratt, Solid State Commun. **25**, 2989 (1978).

<sup>5</sup>A. B. Kunz, Int. J. Quantum Chem. Symp. **15**, 487 (1981).

<sup>6</sup>B. Koiller and L. M. Falicov, J. Phys. C **7**, 299 (1974).

<sup>7</sup>P. W. Anderson, in *Solid State Physics*, edited by F. Seitz and D. Turnbull (Academic, New York, 1963), Vol. 14, p. 99.

<sup>8</sup>B. Koiller and L. M. Falicov, J. Phys. C **8**, 695 (1975).

<sup>9</sup>D. Adler and J. Feinleib, Phys. Rev. B **2**, 3112 (1970).

<sup>10</sup>R. Merlin, T. P. Martin, A. Polian, M. Cardona, B. Andlauer, and D. Tannhauser, J. Magn. Magn. Mater. **9**, 83 (1978).

<sup>11</sup>H. Scheidt, M. Glöbl, and V. Dose, Surf. Sci. **112**, 97 (1981).

<sup>12</sup>S. J. Oh, J. W. Allen, I. Lindau, and J. C. Mikkelsen, Jr., Phys. Rev. B **26**, 4845 (1982).

<sup>13</sup>M. R. Thuler, R. L. Benbow, and Z. Hurych, Phys. Rev. B **27**,

2082 (1983).

<sup>14</sup>T. M. Wilson, Int. J. Quantum Chem. Symp. **3**, 757 (1970).

<sup>15</sup>L. F. Mattheiss, Phys. Rev. B **5**, 290 (1972).

<sup>16</sup>L. F. Mattheiss, Phys. Rev. B **5**, 306 (1972).

<sup>17</sup>O. K. Andersen, H. L. Skriver, H. Nohl, and B. Johansson, Pure Appl. Chem. **52**, 93 (1979).

<sup>18</sup>J. Yamashita and S. Asano, J. Phys. Soc. Jpn. **52**, 3506 (1983).

<sup>19</sup>T. Oguchi, K. Terakura, and A. R. Williams, Phys. Rev. B **28**, 6443 (1983).

<sup>20</sup>T. Oguchi, K. Terakura, and A. R. Williams, J. Appl. Phys. **55**, 2318 (1984).

<sup>21</sup>See Ref. 19, and references therein.

<sup>22</sup>K. Terakura, A. R. Williams, T. Oguchi, and J. Kübler, Phys. Rev. Lett. **52**, 1830 (1984).

<sup>23</sup>S. Hüfner and G. K. Wertheim, Phys. Rev. B **7**, 5086 (1973).

<sup>24</sup>K. Terakura and A. R. Williams (unpublished).

<sup>25</sup>A. R. Williams, J. Kübler, and C. D. Gelatt, Jr., Phys. Rev. B **19**, 6094 (1979).

<sup>26</sup>V. L. Moruzzi, J. F. Janak, and A. R. Williams, *Calculated Electronic Properties of Metals* (Pergamon, New York, 1978).

- <sup>27</sup>The band-energy contribution to the stabilization of AF II due to the intersublattice hybridization is cancelled to some extent by the change in the exchange energy  $-(I/4)M_{\text{loc}}^2$  ( $I$ , intra-atomic exchange integral;  $M_{\text{loc}}$ , magnitude of local magnetic moment), because the stronger intersublattice hybridization generally reduces  $M_{\text{loc}}$  more. Detailed discussions of this aspect in the case of Heusler alloys were given in J. Kübler, A. R. Williams, and C. B. Sommers, *Phys. Rev. B* **28**, 1745 (1983).
- <sup>28</sup>M. T. Hutchings and E. J. Samuelsen, *Solid State Commun.* **9**, 1011 (1971).
- <sup>29</sup>W. L. Roth, *Phys. Rev.* **110**, 1333 (1958).
- <sup>30</sup>J. Kanamori, *Prog. Theor. Phys.* **17**, 177 (1957); **17**, 197 (1957).
- <sup>31</sup>T. Moriya, *Prog. Theor. Phys.* **33**, 157 (1965).
- <sup>32</sup>K. Yosida, A. Okiji, and S. Chikazumi, *Prog. Theor. Phys.* **33**, 559 (1965).
- <sup>33</sup>P. B. Coqblin and A. Blandin, *Adv. Phys.* **17**, 281 (1968).
- <sup>34</sup>J. F. Janak, *Phys. Rev. B* **16**, 255 (1977).
- <sup>35</sup>O. Gunnarsson, *J. Phys. F* **6**, 587 (1976).
- <sup>36</sup>In most of the Mott-insulator theories, the value of  $U - J$  is assumed to be about 10 eV. However, as discussed in the Introduction and in Sec. III, some experimental data suggest that  $U - J$  must be only about 2 eV.
- <sup>37</sup>J. F. Janak and A. R. Williams, *Phys. Rev. B* **23**, 6301 (1981).
- <sup>38</sup>B. E. F. Fender, A. J. Jacobson, and F. A. Wedgwood, *J. Chem. Phys.* **48**, 990 (1968).
- <sup>39</sup>H. A. Alperin, *J. Phys. Soc. Jpn. Suppl. B* **17**, 12 (1962).
- <sup>40</sup>D. C. Khan and R. A. Erickson, *Phys. Rev. B* **1**, 2243 (1970).
- <sup>41</sup>The atomic radius for each atom is determined by using the atomic volume  $V_i$  and the bulk modulus  $B_i$  obtained by the band-structure calculation for each elemental material. The volume difference is allotted according to  $\Delta V_1/\Delta V_2 = (B_2/B_1)(V_1/V_2)$ , so that the given lattice parameter is reproduced.
- <sup>42</sup>L. Pauling, *Nature of the Chemical Bond* (Cornell University Press, Ithaca, 1945).
- <sup>43</sup>V. Heine, *Phys. Rev.* **153**, 673 (1967).